BROAD-BAND ANTIREFLECTION COATINGS FOR
IMPROVED GRATING-EXTERNAL-CAVITY
DIODE LASER PERFORMANCE

BROAD-BAND ANTIREFLECTION COATINGS FOR IMPROVED GRATING-EXTERNAL-CAVITY DIODE LASER PERFORMANCE

By

LIQIANG GUO, B.SC.

A Thesis

Submitted to the School of Graduate Studies

in Partial Fulfillment of the Requirements

for the Degree

Master of Applied Science

McMaster University

MASTER OF APPLIED SCIENCE (2002) McMaster University

(Engineering Physics) Hamilton, Ontario

TITLE: Broad-band Antireflection Coatings for Improved Grating-External-Cavity Diode Laser Performance

AUTHOR: Liqiang Guo, B.Sc. (Shandong University, Jinan, China)

SUPERVISORS: Professor D.T.Cassidy, and Professor P.Mascher

NUMBER OF PAGES: xi, 132

ABSTRACT

In this thesis, strong optical feedback is utilized to realize broad-band wavelength tuning and to stabilize the frequency of a semiconductor diode laser in a grating-external-cavity (GEC) configuration.

To reach the regime of strong optical feedback, the laser facet through which the feedback occurs has to be antireflection (AR) coated. Multi-layer AR coatings were designed using SiO_2, Si_3N_4, SiO_xN_y, and a:Si for specific laser waveguide structures, and were fabricated by an electron cyclotron resonance, plasma enhanced, chemical vapor deposition (ECR-PECVD) system. The film thickness and refractive index were monitored by *in situ* ellipsometry during the deposition. This scheme permitted very low reflectivities, in the order of 5×10^{-4}, to be readily and reproducibly obtained. The diode laser thus obtained was used in a strong feedback configuration. Light emitted from the coated facet was collimated and fed back onto the laser cavity after being reflected off a diffraction grating. The diffraction grating provides frequency selectivity, which is a desirable feature for obtaining a stable single longitudinal mode laser. The laser in this configuration oscillated in a single mode with a greater than 30 dB side mode suppression ratio and a wide tuning range.

ACKNOWLEDGEMENTS

I would like to express my gratitude to my supervisors, Dr. D.T.Cassidy and Dr. P.Mascher, for their guidance and support throughout the course of this work. I especially benefited from their diverse insights in every aspect of this work.

I would like to thank Cristina Simionescu for showing me the way around the lab during the first several months of my studies at McMaster, and Michael Brennan for leading me the way to this project. I would especially like to thank Dr. Zhilin Peng for his invaluable contributions to many scientific aspects of this work. I would also like to thank Sean Woothword and Aaron Vandermeer who generously provided the quantum well lasers described in this thesis.

I would like to thank Dr. Jacek Wojcik for assisting the thin-film depositions on the ECR-PECVD system, and Dr. Tao Yin, Dr. Daizong Li, Dr. Weihong Jiang, and Dr. Yanli Shi for many helpful conversations. Many thanks to Dr. Richard Sobiestijankas, who facilitated me and kindly provided the measuring system.

My wife and my son deserve the most thanks of all. Without their love, I would not have been able to see this work to a successful completion.

Finally, special thanks go to my parents for their support and encouragement during the past years.

Contents

List of Figures

List of Tables

CHAPTER 1

INTRODUCTION

Semiconductor diode lasers were first reported in 1962, shortly after the first demonstrations of other laser types. After the development of high-performance AlGaAs/GaAs double-heterostructure lasers around 1970, this laser structure became a commercial product in the late 1970s offering a number of advantages, including size, power-conversion efficiency, direct-current pumping, reliability, and wavelength flexibility.

Since a number of performance characteristics (e.g., power, modulation speed, spectral linewidth, operating wavelength) can be optimized for specific applications, diode lasers find a large number of applications. For applications that require wavelength tuning, the wide spectral gain normally available in diode lasers is particularly interesting. After the successful development of InGaAsP/InP single-mode diode lasers around 1.3μm and 1.55μm in the early 1980s, therefore, the realization of wavelength-tunable diode lasers became an important issue [1]. This research has mainly been driven by the increasing demand on transmission capacity in optical communications systems, making the application of advanced transmission techniques necessary. This particularly comprises wavelength division multiplexing (WDM) techniques and coherent optical detection schemes [2].

In most of the advanced applications, laser spectroscopy, coherent optical communications, sensing, and precision measurement are the major areas of applications where tunable diode lasers are used. Among the required device characteristics, the tuning range, optical power, spectral linewidth, and FM modulation bandwidth are most important.

The tuning range represents the most specific parameter for a tunable diode laser. Accordingly, the width of the tuning range improves the laser suitability in all practical applications. In most applications, the optical power is also important. This implies a demand for a constant optical power throughout the tuning range.

External-cavity diode lasers have attracted much attention because they have a narrow linewidth and tunable single frequency output, and have been widely used in many applications including coherent communications, interferometric sensors, and spectroscopy [3]. In usual external-cavity diode lasers, a dielectric antireflection (AR) coating on the facet of a diode laser is frequently executed for strong external feedback [4].

Broad-band tunability could be achieved for diode lasers using techniques of quantum-well (QW) engineering. The various schemes include using a single QW, identical multiple QWs (MQWs), and non-identical MQWs [5,6]. Using a diode laser with a properly designed sequence of non-identical

MQWs made of InGaAsP/InP materials, the external-cavity diode lasers can exhibit an extremely broad-band tuning range.

During the past decades, plasma enhanced chemical vapor deposition (PECVD) has been increasingly used for the fabrication of transparent dielectric optical films and coatings [7]. This involves single-layer, multi-layer, graded index, and nanocomposite optical thin-film systems for applications such as optical filters, antireflection (AR) coatings, optical waveguides, and others. PECVD of optical films offers many important advantages compared to other techniques, such as high deposition rate at low ambient temperature, superior mechanical performance in terms of adhesion, stress, and hardness, flexible control of gas composition allowing one to deposit multi-layer interference optical systems.

The main objectives of this thesis are:

1. Select a suitable optical feedback configuration, with the amount of optical feedback being critical. Consideration must be given to what is experimentally feasible.
2. For strong optical feedback, determine a technique for optical coating and obtaining the lowest reflectivity with the widest possible bandwidth. It is necessary to antireflection coat one of the laser facets.
3. Design broad-band, multi-layer AR coatings. Determine the optical properties of the materials being used in AR coating designs.

4. The effective refractive index of ridge-waveguide MQW lasers, serving as the substrate in AR coating designs, should be determined precisely.
5. Build the external-cavity diode laser using a diffraction grating for the external wavelength-selective reflector.
6. Verify that a diode laser can oscillate in a single longitudinal mode, i.e., has a side mode suppression ratio of greater than 30dB, and measure the tuning range of wavelength, over which single mode oscillation is obtained.

I did my best to organize the thesis into a logical sequence of chapters. After the short introduction of this chapter, the basic principles of optical waveguides are reviewed in Chapter 2. Chapter 2 also includes an introduction of material properties of $In_{1-x}Ga_xAs_yP_{1-y}$. In Chapter 3, the theoretical principles and background of AR coatings are reviewed, and the design algorithm of AR coatings for ridge waveguide MQW diode lasers is discussed.

The fabrication of AR coatings by ECR-PECVD is presented in Chapter 4, followed by the controls of film thickness and refractive index by *in situ* ellipsometry. Optical properties of SiO_2, Si_3N_4, SiO_xN_y, and a:Si, which were used as coating materials, are also summarized in this chapter.

In Chapter 5, grating-external-cavity (GEC) diode lasers are presented, followed by experimental results in this work. Thesis summary and conclusions are given in Chapter 6.

CHAPTER 2

OPTICAL WAVEGUIDE AND EFFECTIVE REFRACTIVE INDEX FOR InGaAsP/InP RIDGE WAVEGUIDE STRUCTURE

2.1 INTRODUCTION

In the past decades, III-V compounds (which consist of elements from columns III and V of the periodic table) have emerged as the materials of choice for lasers that emit in the 0.7~1.6 μm wavelength ranges. These ranges include the important fiber-optic communication bands at 0.85, 1.30, and 1.55 μm, the pumping bands for fiber amplifiers at 0.98 and 1.48 μm, the window for pumping Nd-doped YAG at 0.81 μm, and the wavelength used for optical disk players at 0.78 μm. Most of these materials have a direct gap in *E-k* space, which means that the minimum and maximum of the conduction and valence bands, respectively, fall at the same *k*-value. This facilitates radiative transitions because momentum conservation is naturally satisfied by the annihilation of the equal and opposite momenta of the electron and hole (the momentum of the photon

$\hbar k = \hbar\omega/c = E_{ph}/c$ is negligibly small due to the high value for the speed of light $c = 2.997925 \times 10^{10}\ cm/s$).

Among the most important material systems for III-V semiconductor lasers are AlGaAs on GaAs substrate and InGaAsP on InP substrate. While AlGaAs/GaAs covers the wavelength range below 0.9 μm, the InGaAsP/InP material system gains importance for light sources and detectors in the 1.20 ~ 1.67 μm wavelength regime. Therefore the wavelengths with minimal dispersion in optical fibers at 1.30 μm and minimal absorption at 1.55 μm can be covered with InGaAsP/InP diode lasers.

In this work, ridge waveguide InGaAsP/InP MQW lasers of different emission wavelengths were used. The determination of the effective refractive index of the diode laser, which is the key in AR coating designs, is discussed and then calculated in this chapter. Also presented in this chapter are the optical properties of the InGaAsP/InP material system. Computer programs were developed to facilitate all the calculations.

2.2 REFRACTIVE INDEX OF $In_{1-x}Ga_xAs_yP_{1-y}$

$In_{1-x}Ga_xAs_yP_{1-y}$ lattice-matched to InP can be achieved if the gallium and arsenic mole fractions x and y, respectively, are chosen such that [8]:

$$x = \frac{0.1894y}{0.4184 - 0.013y} \tag{2.1}$$

The bandgap energy of $In_{1-x}Ga_xAs_yP_{1-y}$ depends on x and y in a good approximation as [8]:

$$E_g\,[\text{eV}] = 1.35 + 0.668x - 1.068y + 0.758x^2 + 0.078y^2 - 0.069xy - 0.322x^2y + 0.03xy^2 \quad \text{at 300K} \qquad (2.2)$$

Correspondingly, the bandgap wavelength:

$$\lambda_g\,[\mu\text{m}] \approx \frac{1.24}{E_g} \qquad (2.3)$$

The above calculation is based on the assumption that carrier recombination occurs directly at the bandgap of the quaternary. In practice, several mechanisms can cause carrier recombination slightly away from the quaternary bandgap, such as carrier-induced bandgap change, doping level, working temperature and strain. Among them, carrier-induced change is the major contribution to the change of the refractive index of $In_{1-x}Ga_xAs_yP_{1-y}$ [9,10].

The refractive index in compound semiconductors below the band edge can be best represented by the modified single-effective oscillator (MSEO) model [11]. Restricting the analysis to the transparent wavelength region, which means that the refractive indices of the active regions may not be covered, the bandgap energy E_g and the single oscillator energies for $In_{1-x}Ga_xAs_yP_{1-y}$

$$E_0\,[\mathrm{eV}] = 3.391+0.524x-1.891y+1.626xy+0.595x^2(1-y) \qquad (2.4)$$

$$E_d\,[\mathrm{eV}] = 28.91+7.54x+(12.36x-12.71)y \qquad (2.5)$$

are required to calculate the refractive index for the photon energy E [12]:

$$\mathrm{n}(E) = \sqrt{1+\frac{E_d}{E_0}+\frac{E_d E^2}{E_0^3}+\frac{\eta\, E^4}{\pi}\ln\left(\frac{2E_0^2-E_g^2-E^2}{E_g^2-E^2}\right)} \qquad (2.6)$$

where

$$\eta = \frac{\pi\, E_d}{2E_0^3(E_0^2-E_g^2)} \qquad (2.7)$$

and $E = \hbar\omega$ is the photon energy.

Using the lasing wavelength and bandgap wavelength instead of E and E_g by way of Eq(2.3), respectively, the refractive index of $\mathrm{In_{1-x}Ga_xAs_yP_{1-y}}$ lattice-matched to InP can be calculated. The dependence of E_g on the mole fractions x and y is taken from Eq(2.2), and lattice-matching links the mole fractions by Eq(2.1). It should be noted that the accuracy of this model deteriorates at energies approaching the band edge because of the strong dispersion near the absorption edge.

Burkhard [13] showed that for symmetrical waveguides with a quaternary active layer and InP claddings, the phase index of the quaternary lattice-matched to InP near the bandgap region is:

$$n_Q(\Delta E,y) = 3.425+0.94\Delta E+0.952(\Delta E)^2 +(0.255-0.257\Delta E)y-(0.103-0.092\Delta E)y^2 \qquad (2.8)$$

where ΔE is the energy separation below the respective band gaps in analogy to Vegard's rule for the lattice parameter of an alloy, $-0.2\text{eV} \leqslant \Delta E \leqslant 0$. The corresponding index describing the group index

$$n_{Q,\text{group}}(\Delta E,y) = n_Q+E(dn_Q/dE)$$

obtained from Eq(2.8) is:

$$n_{Q,\text{group}}(\Delta E,y) = 3.425+1.88\Delta E+2.86(\Delta E)^2+(0.255-0.514\Delta E)y -(0.103-0.184\Delta E)y^2+0.94E+1.9\Delta E-0.257Ey+0.092Ey^2 \qquad (2.9)$$

Bennett *et al.* [9] investigated the carrier-induced change in refractive index Δn of InGaAsP, and showed that three carrier effects could give substantial contributions to the refractive index near the direct gap of III-V semiconductors. The bandfilling (Burstein-Moss effect) decreases absorption for energies near the bandgap. Bandgap shrinkage increases absorption, but the effect does not extend to energies below the new bandgap. Free-carrier absorption, however, increases as λ^2 and dominates the loss at energies below the bandgap. Because of the λ^2 dependence, the free-carrier absorption (also known as plasma effect) increases as the photon energy is decreased below the bandgap. It has been shown that the contribution to the changes in refractive index due to the plasma effect only becomes important at quite large concentrations [14]. On the other hand, both the bandfilling and bandgap shrinkage effects on the refractive index are largest near the bandgap and approach zero for $E << E_g$. The bandfilling effect is partly compensated by bandgap shrinkage due to carrier interaction at high concentrations. The bandfilling and free-carrier absorption effects both produce a negative Δn for wavelengths in the transparent regime of the semiconductors; band-gap shrinkage produces a positive Δn in the same regime. Considering the compensating effects of bandgap shrinkage and bandfilling, Botteldooren and Baets [10] presented a more accurate method by introducing bandgap shrinkage into the model for the carrier-induced refractive index change. In the range of 10^{15}/cm^3 – 10^{19}/cm^3 they found that the bandgap shrinkage (ΔE in Eq(2.8) and Eq(2.9)) is well represented by:

$$\Delta E = -\frac{\Delta E_g m_e^{1/2}}{\varepsilon_r} \tag{2.10}$$

with

$$\Delta E_g = \frac{A n_1^{\alpha} + B n_1^{1/3}}{1 + n_0 / n_1} \tag{2.11}$$

where $n_1 = n/m_e^{3/2}$, n is the particle concentration per cm^3, m_e is the effective mass [8]:

$$m_e/m_0 = 0.08-0.116x+0.026y-0.059xy$$
$$+(0.064-0.02x)y^2+(0.06+0.032y)x^2 \qquad (2.12)$$

where m_0 is the free-electron mass, x and y are the gallium and arsenic mole fraction, respectively. A, B, α, and n_0 are fitting parameters. They are A=1.04×10^3, B=2.80×10^{-7}, α= -0.19, n_0=2.40×10^{19}. ε_r is the relative dielectric constant, found to be [15]:

$$\varepsilon_r(y) = 12.40+1.5y \qquad (2.13)$$

for $In_{1-x}Ga_xAs_yP_{1-y}$ lattice-matched to InP.

Based on above discussions, the refractive index of the InGaAsP/InP material system can be determined once the MQW laser structure is given.

2.3 OPTICAL WAVEGUIDE THEORY

An optical waveguide is a medium which transports electromagnetic energy from one point in space to another. They are commonly used to confine optical fields near a device's active region or to interconnect elements in an optoelectronic circuit. The optical confinement is achieved by using a multi-layered material structure containing a core region of higher refractive index relative to the surrounding cladding layers. As will be described below, electromagnetic radiation propagates through the waveguide as a set of discrete spatial energy distributions known as optical modes. To calculate these allowed modes, two dimensional mode solvers are usually employed [16].

2.3.1 The Two Dimensional Slab Waveguides

To begin the discussion of a 2-D optical waveguide it is useful to examine Maxwell's equations in an isotropic, lossless dielectric medium:

$$\nabla \times \boldsymbol{E} = -\mu_0 \frac{\partial \boldsymbol{H}}{\partial t} \tag{2.14}$$

and

$$\nabla \times \boldsymbol{H} = \varepsilon_0 n^2 \frac{\partial \boldsymbol{E}}{\partial t} \tag{2.15}$$

where ε_0 and μ_0 are the dielectric permittivity and magnetic permeability of free space, respectively, and n is the refractive index. In the orthogonal coordinate system (x,y,z), suppose that the plane wave propagates along the z direction with the propagation constant β. The electromagnetic fields vary as:

$$\boldsymbol{E} = E(x,y) \cdot e^{j(\omega t - \beta z)} + c.c \tag{2.16}$$

and

$$\boldsymbol{H} = H(x,y) \cdot e^{j(\omega t - \beta z)} + c.c \tag{2.17}$$

where the angular frequency $\omega = 2\pi c / \lambda$, and c is the light velocity in free space ($c = 1/\sqrt{\varepsilon_0 \mu_0}$).

In the step-index 2-D slab waveguide shown in Figure 2.1, the electromagnetic fields are independent of y. Accordingly, since $\partial / \partial t = j\omega$, $\partial / \partial z = -j\beta$ and $\partial / \partial y = 0$, Eq(2.14) and Eq(2.15) yield two different modes with mutually orthogonal polarization states. One is the *TE* mode, which consists of the field components E_y, H_x, and H_z. The other is the *TM* mode, which has E_x, H_y, and E_z.

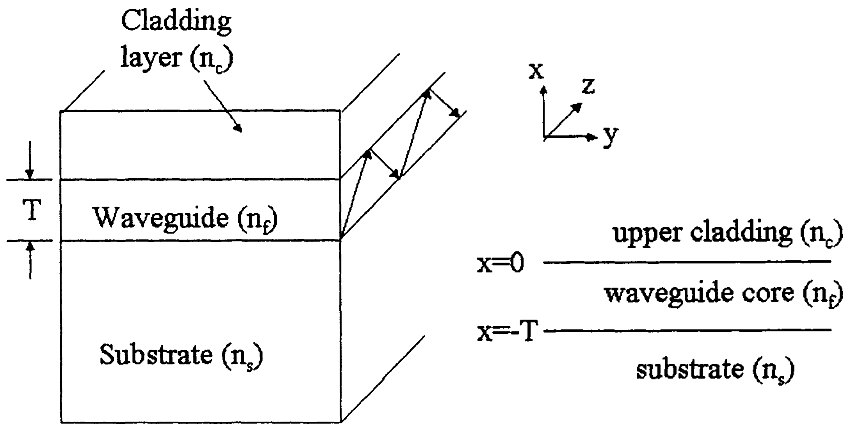

(a) Basic optical-waveguide structure

(b) A three-layer planar slab waveguide

Figure 2.1 2-D optical waveguides

Wave equations for the *TE* and *TM* modes are:

<u>*TE* mode</u>

$$\frac{\partial^2 E_y}{\partial x^2} + (k_0^2 n^2 - \beta^2) E_y = 0 \tag{2.18}$$

$$\begin{cases} H_x = -\dfrac{\beta}{\omega \cdot \mu_0} E_y \\ H_z = -\dfrac{1}{j\omega \cdot \mu_0} \dfrac{\partial E_y}{\partial x} \end{cases} \tag{2.19}$$

TM mode

$$\frac{\partial^2 H_y}{\partial x^2} + (k_0^2 n^2 - \beta^2) H_y = 0 \tag{2.20}$$

$$\begin{cases} E_x = \dfrac{\beta}{\omega \cdot \varepsilon_0 n^2} H_y \\ E_z = \dfrac{1}{j\omega \cdot \varepsilon_0 n^2} \dfrac{\partial H_y}{\partial x} \end{cases} \tag{2.21}$$

The field solutions and the boundary conditions at the interfaces $x = -T$ and $x = 0$ lead to eigenvalue equations that determine the propagation characteristics of the *TE* and *TM* modes.

The two orthogonal *TE* and *TM* modes must be distinguished to discuss dispersion characteristics of the guided modes. Only the *TE* mode is discussed here, because a similar analysis can be made for the *TM* mode. From Eq(2.18), the field solutions can be written in the form [17]:

$E_y = E_c \exp(-\gamma_c x)$, $x>0$ (in the cladding layer) (2.22a)

$E_y = E_f \cos(k_x x + \phi_c)$, $-T<x<0$ (in the guiding layer) (2.22b)

$E_y = E_s \exp(\gamma_s (x+T))$, $x<-T$ (in the substrate) (2.22c)

where the propagation constants in the x direction are expressed in terms of the effective index N_e, where $\beta = N_e \cdot k_0$, in the following expressions:

$$\gamma_c^2=k_0^2(N_e^2-n_c^2) \tag{2.23a}$$

$$k_x^2=k_0^2(n_f^2-N_e^2) \tag{2.23b}$$

$$\gamma_s^2=k_0^2(N_e^2-n_s^2) \tag{2.23c}$$

The boundary condition that the tangential field components E_y, and H_z are continuous at the interface $x=0$ yields:

$$E_c=E_f\cos\phi_c\,, \qquad \tan\phi_c=\gamma_c/k_x \tag{2.24}$$

similarly,

$$E_s=E_f\cos(k_xT-\phi_c), \qquad \tan(k_xT-\phi_c)=\gamma_c/k_x \tag{2.25}$$

at $x=-T$.

Eliminating arbitrary coefficients ϕ_c in the preceding relations results in an eigenvalue equation:

$$k_xT=(m+1)\,\pi-\tan^{-1}(k_x/\gamma_s)-\tan^{-1}(k_x/\gamma_c) \tag{2.26}$$

where $m=0,1,2,\ldots$, denotes the mode number.

When the indices of the waveguide materials and the guide thickness T are given, k_x can be obtained from Eq(2.26). Substitution of k_x into Eq(2.23) results in the effective index N_e of the guided mode. N_e must be discrete values in the range of $n_s < N_e < n_f$ because the mode number is a positive integer. In other words, zig-zag rays with certain incident angles can propagate as guided modes along the guiding layer. Among some guided modes, the fundamental mode with the mode number 0 has the largest effective index corresponding to the ray with the angle closest to 90 degree.

When the waveguide parameters are given, the transcendental Eq(2.26) can be solved numerically to evaluate dispersion characteristics of guided modes. Such a numerical evaluation is applicable to any step-index 2-D waveguide by introducing the following normalizations:

$V = k_0 T\sqrt{n_f^2 - n_s^2}$ normalized frequency (2.27)

$b_E = (N_e^2 - n_s^2)/(n_f^2 - n_s^2)$ normalized guide index (2.28)

$a_E = (n_s^2 - n_c^2)/(n_f^2 - n_s^2)$ asymmetry measure (2.29)

When $n_s = n_c$, $a_E = 0$, this implies symmetrical waveguides. However, 2-D waveguides are generally asymmetrical waveguides. Using definitions (2.27) to (2.29), Eq(2.26) can be rewritten in the normalized form:

$$V\sqrt{1-b_E} = (m+1)\pi - \tan^{-1}\sqrt{\frac{1-b_E}{b_E}} - \tan^{-1}\sqrt{\frac{1-b_E}{b_E + a_E}} \tag{2.30}$$

From Eq(2.30), the value of V_m at the cutoff of the guided modes is given by:

$$V_m = V_0 + m\pi , \qquad V_0 = \tan^{-1}\sqrt{a_E} \tag{2.31}$$

V_0 is the cutoff value for the fundamental mode.

If the normalized frequency V of the waveguide ranges over $V_m < V < V_{m+1}$, the TE_0, TE_1, ... and TE_m modes are supported, and the number of guided modes is $m+1$. For symmetrical waveguides ($n_s=n_c$), $V_0=0$. This implies that the fundamental mode is not cutoff in a symmetrical waveguide.

For the *TM* modes, the analysis is similar to the preceding. The resulting normalized eigenvalue equation is:

$$V\left\{\sqrt{q_s}\left(\frac{n_f}{n_s}\right)\right\}\sqrt{1-b_M} = (m+1)\pi - \tan^{-1}\sqrt{\frac{1-b_M}{b_M}} - \tan^{-1}\sqrt{\frac{1-b_M}{b_M + a_M(1-b_M d)}} \tag{2.32}$$

with:

$$b_M = \left(\frac{N_e^{\,2} - n_s^2}{n_f^2 - n_s^2}\right)\left(\frac{n_f}{n_s q_s}\right) \tag{2.33a}$$

$$q_s = \left(\frac{N_e}{n_f}\right)^2 + \left(\frac{N_e}{n_s}\right)^2 - 1 \tag{2.33b}$$

$$a_M = \left(\frac{n_f}{n_c}\right)^4\left(\frac{n_s^2 - n_c^2}{n_f^2 - n_s^2}\right) \tag{2.33c}$$

$$d = \left\{1 - \left(\frac{n_s}{n_f}\right)^2\right\}\left\{1 - \left(\frac{n_c}{n_f}\right)^2\right\} \tag{2.33d}$$

For the *TM* modes, although the eigenvalue equation has been normalized, numerical solutions are not obtained unless index ratios (n_s/n_f) and (n_c/n_f) are given.

At this point, computer codes were written in MATLAB 5.20 to help solve the transcendental Eq(2.30) and Eq(2.32) once all the parameters were known. The codes are presented in detail in Appendix A.

2.3.2 Multi-layer Slab Waveguides

Waveguides containing more than three layers are frequently used for many semiconductor devices. Analytical solutions become very complex for these structures and alternative approaches should be followed. The propagation properties of optical planar waveguides with multi-layer index profiles can be best analyzed by the transfer matrix of transmitted and reflected beam amplitudes in multiple layers, the so called "zero-transfer matrix element method" [18], which is described briefly in the following.

The propagation wave number for guided-wave modes is obtained from the condition that certain elements in the transfer matrix must be zero. This numerical technique can be implemented for slab waveguides containing an arbitrary number of layers, and can be easily applied to the calculation of both *TE* and *TM* modes. For brevity, only *TE* solutions will be discussed here. The analysis is similar for *TM* solutions.

A multi-layer slab waveguide structure is shown in Figure 2.2. Each layer is assumed to have a uniform thickness and refractive index profile.

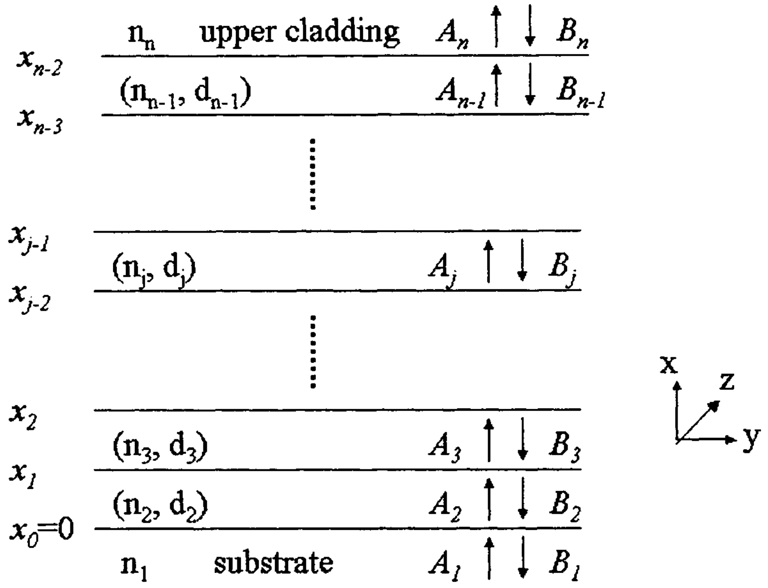

Figure 2.2 General form of multi-layer slab waveguide structure. A_j and B_j are the amplitudes of forward- and backward-propagation components of the electric field. Each layer (j) is of uniform index n_j. d_j is the j^{th} layer thickness. Light propagation is assumed to be in the z-direction.

For *TE* polarized light, the electric field in the j^{th} layer must satisfy the wave equation:

$$\frac{d^2 E_{y,j}(x)}{dx^2} + \left(n_j^2 k_0^2 - \beta^2\right) E_{y,j}(x) = 0 \tag{2.34}$$

and have the general form [18]:

$$E_{y,j}(x) = A_j \exp[-P_{x,j}(x - x_{j-2})] + B_j \exp[P_{x,j}(x - x_{j-2})] \tag{2.35}$$

where

$$P_{x,j} = \sqrt{\beta^2 - n_j^2 k_0^2} \tag{2.36}$$

A_j and B_j ($j=1,2,\ldots, n$) are the amplitudes of forward- and backward-propagation components of the electric field. n_j is the refractive index of the j^{th} layer and x_j represents the position or the interface between $(j+1)^{\text{th}}$ and $(j+2)^{\text{th}}$ layer.

A similar expression for the z-component of the magnetic field H_z can be found:

$$-i\omega\cdot\mu_0 H_{z,j}(x) = -P_{x,j}A_j\exp[-P_{x,j}(x-x_{j-2})] + P_{x,j}B_j\exp[P_{x,j}(x-x_{j-2})] \tag{2.37}$$

Eq(2.36) and Eq(2.37) can be combined in a matrix equation:

$$\begin{bmatrix} E_{y,j} \\ -i\omega\cdot\mu_0 H_{z,j} \end{bmatrix} = \begin{bmatrix} \exp[-P_{x,j}(x-x_{j-2})] & \exp[P_{x,j}(x-x_{j-2})] \\ -P_{x,j}\exp[-P_{x,j}(x-x_{j-2})] & P_{x,j}\exp[P_{x,j}(x-x_{j-2})] \end{bmatrix} \cdot \begin{bmatrix} A_j \\ B_j \end{bmatrix} \tag{2.38}$$

The tangential field components in the j^{th} layer are matched at the upper and lower interfaces according to the boundary conditions. At the upper interface ($x=x_{j-1}$) we have:

$$\begin{bmatrix} E_y \\ -i\omega\cdot\mu_0 H_z \end{bmatrix} = \begin{bmatrix} \exp[-P_{x,j}(x_{j-1}-x_{j-2})] & \exp[P_{x,j}(x_{j-1}-x_{j-2})] \\ -P_{x,j}\exp[-P_{x,j}(x_{j-1}-x_{j-2})] & P_{x,j}\exp[P_{x,j}(x_{j-1}-x_{j-2})] \end{bmatrix} \cdot \begin{bmatrix} A_j \\ B_j \end{bmatrix} \tag{2.39}$$

and, at the lower boundary ($x=x_{j-2}$):

$$\begin{bmatrix} E_y \\ -i\omega \cdot \mu_0 H_z \end{bmatrix} = \begin{bmatrix} 1 & 1 \\ -P_{x,j+1} & P_{x,j+1} \end{bmatrix} \cdot \begin{bmatrix} A_{j+1} \\ B_{j+1} \end{bmatrix} \tag{2.40}$$

Combining Eq(2.39) and Eq(2.40) yields:

$$\begin{bmatrix} A_{j+1} \\ B_{j+1} \end{bmatrix} = M_j \begin{bmatrix} A_j \\ B_j \end{bmatrix} \tag{2.41}$$

where the transfer matrix M_j is defined as:

$$M_j = \begin{bmatrix} 1 & 1 \\ -P_{x,j+1} & P_{x,j+1} \end{bmatrix}^{-1} \cdot \begin{bmatrix} \exp[-P_{x,j}(x_{j-1} - x_{j-2})] & \exp[P_{x,j}(x_{j-1} - x_{j-2})] \\ -P_{x,j} \exp[-P_{x,j}(x_{j-1} - x_{j-2})] & P_{x,j} \exp[P_{x,j}(x_{j-1} - x_{j-2})] \end{bmatrix} \tag{2.42}$$

Using an iteration process, the amplitudes of the field components in n^{th} layer can be related to those in the first layer. The resulting expression is given as:

$$\begin{bmatrix} A_n \\ B_n \end{bmatrix} = \begin{bmatrix} \alpha_1 & \alpha_2 \\ \alpha_3 & \alpha_4 \end{bmatrix} \cdot \begin{bmatrix} A_1 \\ B_1 \end{bmatrix} \tag{2.43}$$

where

$$\begin{bmatrix} \alpha_1 & \alpha_2 \\ \alpha_3 & \alpha_4 \end{bmatrix} = M_{n-1} \cdot M_{n-2} \cdots\cdots M_2 \cdot M_1 \tag{2.44}$$

For guided modes, there should be no forward-propagating wave in the substrate and no backward-propagating wave in the cladding layer. In order to satisfy this condition, B_n (the backward-wave amplitude in the cladding layer $j=n$) and A_1 (the forward-wave amplitude in the substrate $j=1$) obviously should be zero:

$$\begin{bmatrix} A_n \\ 0 \end{bmatrix} = \begin{bmatrix} \alpha_1 & \alpha_2 \\ \alpha_3 & \alpha_4 \end{bmatrix} \cdot \begin{bmatrix} 0 \\ B_1 \end{bmatrix} \tag{2.45}$$

Eq(2.45) can be satisfied only if the element α_4 of the matrix is equal to zero. This is the origin of the so called "zero-transfer matrix element method"

From above analyses, one can see that α_4 is a function of β/k, the guide-normalized propagation constant in the *z*- direction. The waveguide may be characterized in terms of the normalized propagation constant (β/k) as a function of layer thickness as well as of the refractive indices of the layers. Therefore, Eq(2.45) is an eigenvalue equation which can be used to calculate the propagation constants β for the given modes of the waveguide structure.

2.3.3 3-D Optical Waveguides and Effective Index Method

Semiconductor waveguide devices usually require optical confinement in both the vertical and lateral directions. However, solving for the field distributions in two dimensions is not trivial. The guided modes in 3-D waveguides cannot be simply classified as *TE* or *TM* as in the 2-D case, but are hybrid in nature, containing aspects of each. Generally, they are classified into one of two categories: E_{pq}^{y} modes having main electromagnetic field components E_y and H_x (resembling *TE* modes in the slab waveguide) and E_{pq}^{x} modes having dominant E_x and H_y components (resembling *TM* modes in the slab waveguide). The subscripts p and q represent the mode order or number of lobes in the field distributions in the x and y directions, respectively, where $p,q=1,2,3\ldots$

Exact solutions for 3-D optical waveguides are very difficult to obtain and it is necessary to resort to approximation techniques. One of the more common approaches is known as the "effective index method" [19] which offers the advantage of simplicity and has been shown to be very accurate for waveguides far above cutoff.

The guiding structure of interest in this work is known as "ridge" waveguide and is illustrated in Figure 2.3(a). This type of waveguide structure is designed to allow the optical mode to evanescently penetrate into the etched ridge material. This has the effect of raising the effective index beneath the ridge which produces lateral confinement of the optical field. The increase in effective index is dependent on the refractive index values and the dimensions of the waveguide layers.

The effective index method is a technique well-suited to analyzing ridge waveguides. It consists of breaking the 3-D structure into two 2-D slab waveguide problems. Figures 2.3(b) and 2.3(c) illustrate the procedure.

First, the multiple quantum wells (MQWs) can be represented by the waveguide core, following the procedure described in Section 2.3.2.

Second, the 3-D waveguide is broken into three distinct regions, each of which is treated as an infinite 2-D slab waveguide. For E_{qp}^{y} modes (having E_y as the dominant component), the procedure described above for solving 2-D slab waveguides can be utilized for *TE* modes in each of the three regions. This analysis will yield the effective refractive indices N_I, N_{II} and N_{III} for regions I, II and III, respectively. In most ridge waveguide designs, symmetry will dictate that $N_I=N_{III}$. Defining $N_I=N_{III}=N_{side}$, the condition for lateral confinement becomes $N_{II} > N_{side}$. The condition for vertical confinement is $n_f > n_c, n_s$.

The third step in the procedure is to turn the slab waveguide shown in Figure 2.3(c) onto its side. The calculated effective refractive indices, N_I, N_{II} and N_{III}, are then used as the layer indices in a three-layer slab waveguide problem. The eigenvalue Eq(2.32) for *TM* modes should now be used to account for the change in waveguide orientation. The total effective index is then found and the field distributions can be obtained.

To obtain the solutions for E_{pq}^{x} modes, a similar analysis can be followed. In this case, the effective indices for *TM* modes are calculated for the three slab waveguide regions. The waveguide is then turned onto its side and the *TE* eigenvalue equation Eq(2.30) should be utilized.

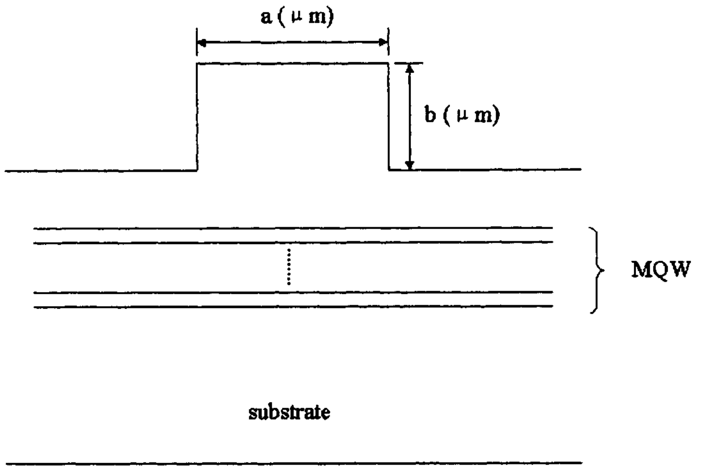

Figure 2.3(a) Physical dimensions of the ridge waveguide MQW laser structure

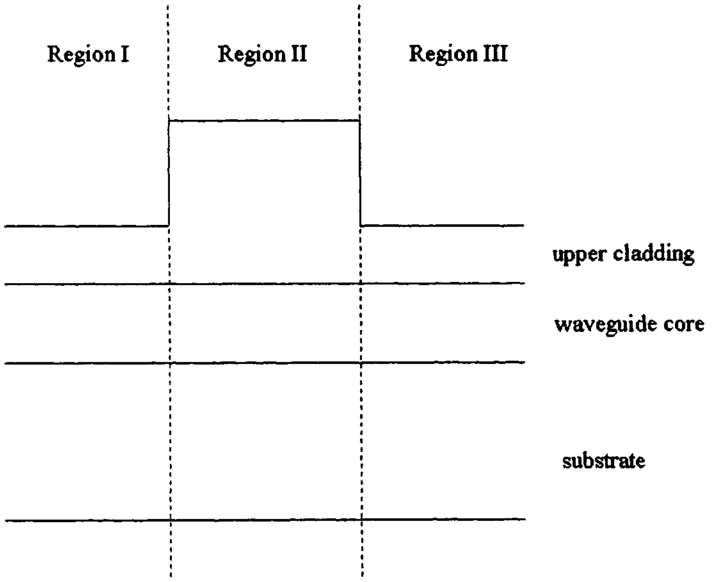

Figure 2.3(b) The 3-D waveguide can be split into three regions. Each region can be treated as a 2-D slab waveguide

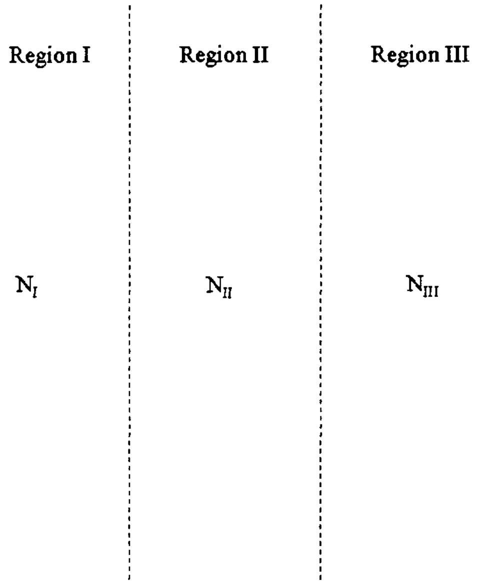

Figure 2.3(c) The effective indices obtained from regions I, II, III are used to construct a three-layer slab waveguide. In most cases, the waveguide structure is horizontally symmetric, therefore the assumption of $N_I=N_{III}$ can be made

2.4 SUMMARY

The effective refractive index for ridge waveguide InGaAsP/InP MQW diode lasers can be determined as follows: First, the refractive indices of each layer in a MQW structure are calculated. Then, the effective refractive index of the multi-layer slab waveguide is calculated based on the "zero-transfer matrix element method". Finally, the "effective index method" is utilized to calculate the effective refractive index for the ridge waveguide structure. The whole procedure is shown in Figure 2.3(a) to (c). Computer programs were written in MATLAB 5.20 to facilitate all the calculations, and presented in Appendix B.

CHAPTER 3

ANTIREFLECTION COATINGS

3.1 INTRODUCTION

Antireflection (AR) coatings are considered one of the key technologies for optoelectronic devices such as semiconductor laser amplifiers (SLAs), external-cavity semiconductor diode lasers, high power lasers and superluminescent light emitting diodes (LEDs). AR coatings with ultra-low reflectivity and broad bandwidth are particularly desirable. For SLAs, less than 10^{-3} reflectivity is needed to suppress Fabry-Perot mode oscillations [20]. For wavelength-tunable external-cavity semiconductor diode lasers, reflectivities of less than 1.5×10^{-4} are required to achieve axial-mode stability [21], and broad gain bandwidth is frequently needed to achieve a stable tuning range. Specifically, the wavelength division multiplexing (WDM) fiber-optic communication systems employing erbium-doped fiber amplifiers (EDFA's) have a bandwidth nearing to 100 nm. The tunable laser sources suitable for testing such systems must have comparable bandwidth.

The most popular approaches to achieving low facet reflectivity in external-cavity diode lasers and optical amplifiers are:

(1) dielectric antireflection coatings [22,23],

(2) tilted gain stripes [24], and

(3) buried facets [25]

In addition, methods (1) and (2) can be combined [26].

One drawback of the tilted-strip approach is that, tilting the laser strip introduces additional complications in the laser processing stage and generally shows improved performance only if the laser facets are additionally AR coated [27].

Another means of facet reflectivity reduction is the use of gain media with buried facets [25]. In these devices the waveguide stops several microns inside the chip, with semi-insulating material between the end of the guide and the facet. The beam expands inside the buried-facet region since there is no waveguiding. Therefore, the reflection at the semiconductor-air interface does not couple strongly back into the waveguide. The reflectance decreases with increasing length of the buried-facet region. However, if the non-guiding region is too long, the internal beam will hit the top-surface metallization, creating a multiple-lobed far-field output and spoiling the ability to couple efficiently to the mode of the external cavity. Therefore, a buried-facet gain medium would probably give poor performance in a simple extended-cavity laser, but they might be useful in either a double-ended external cavity or in ring lasers.

Hence, at the present stage of this project, only multi-layer AR coatings with low reflectivity and broad bandwidth were investigated.

3.2 THEORY OF THIN-FILM OPTICS

Thin-film optics has been studied intensively during the past decades, and there are a number of detailed discussions of their analysis and design [28,29]. In this section, a brief description of these issues will be given, focusing on the applications that have been investigated in this work. The notation of reference [29] will be followed.

The thin-film problems can be solved by Maxwell's equations together with the appropriate material equations [28,29]. A light wave, which is electromagnetic and a homogeneous, plane, plane-polarized harmonic (or monochromatic) wave, may be represented by expressions of the form:

$$E = \mathcal{E}\exp\{i[\omega t - (2\pi N/\lambda)x + \varphi]\} + c.c \tag{3.1}$$

where x is the distance along the direction of propagation, E is electric field vector, $\mathcal{E}$ the electric amplitude and φ an arbitrary phase. N is the complex refractive index,

$$N = n - ik \tag{3.2}$$

where n is the real refractive index and k the extinction coefficient. N is always a function of λ. k is related to the absorption coefficient α by:

$$\alpha = 4\pi k/\lambda \tag{3.3}$$

Similar to Eq(3.1), an expression holds for H, the magnetic field:

$$H = \mathcal{H}\exp\{i[\omega t - (2\pi N/\lambda)x + \varphi']\} + c.c \tag{3.4}$$

The optical admittance is defined as the ratio of the magnetic and electric fields:

$$y = H/E \tag{3.5}$$

and y is usually complex. In free space, y is real and is denoted by $\mathcal{Y}$,

$$\mathcal{Y} = 2.6544 \times 10^{-3}\ \mathrm{S}$$

Then the optical admittance of a medium is connected with the refractive index by:

$$y = N\ \mathcal{Y} \tag{3.6}$$

The simple boundary of plane wave incident on a single surface is sketched in Figure 3.1. At oblique incidence, the idea of a tilted optical admittance η is introduced [29],

$$\eta_p = y/\cos\theta = N\ \mathcal{Y}\ /\cos\theta \tag{3.7}$$

$$\eta_s = y\cos\theta = N\ \mathcal{Y}\ \cos\theta \tag{3.8}$$

where p stands for p-polarized or *TM*, and s stands for s-polarized or *TE*.

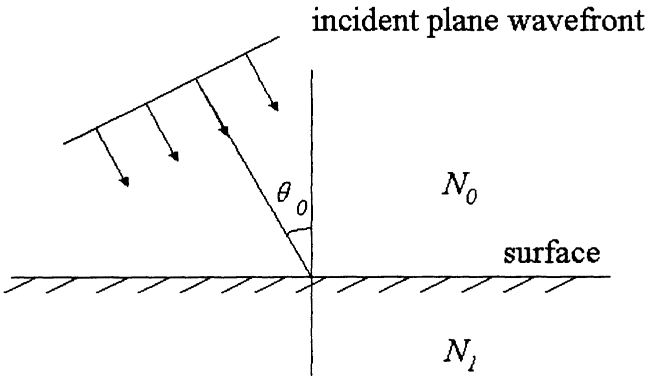

Figure 3.1 Plane wave incident on a single surface

Denoting η_p or η_s by η, for either plane of polarization, the Fresnel amplitude reflection coefficient ρ and transmission coefficient τ can be written

$$\rho = \frac{\eta_0 - \eta_1}{\eta_0 + \eta_1}, \qquad \tau = \frac{2\eta_0}{\eta_0 + \eta_1} \tag{3.9}$$

The reflectance R is defined as the ratio of the reflected and incident intensities, and the transmittance T as the ratio of the transmitted and incident intensities. Then

$$R = \frac{I_r}{I_i} = \rho \cdot \rho^* = \left(\frac{\eta_0 - \eta_1}{\eta_0 + \eta_1}\right)\left(\frac{\eta_0 - \eta_1}{\eta_0 + \eta_1}\right)^*, \tag{3.10a}$$

$$T = \frac{I_t}{I_i} = \frac{\eta_1}{\eta_0}\tau \cdot \tau^* = \frac{4\,\mathrm{Re}(\eta_0)\mathrm{Re}(\eta_1)}{(\eta_0 + \eta_1)(\eta_0 + \eta_1)^*} \tag{3.10b}$$

At normal incidence, $\eta = y = N\mathscr{Y}$, which indicates that the distinction between *TE* and *TM* disappears. Therefore,

$$\rho = \frac{y_0 - y_1}{y_0 + y_1} = \frac{N_0 - N_1}{N_0 + N_1}, \qquad \tau = \frac{2y_0}{y_0 + y_1} = \frac{2N_0}{N_0 + N_1} \tag{3.11}$$

and

$$R = \left(\frac{y_0 - y_1}{y_0 + y_1}\right)\left(\frac{y_0 - y_1}{y_0 + y_1}\right)^* = \left(\frac{N_0 - N_1}{N_0 + N_1}\right)\left(\frac{N_0 - N_1}{N_0 + N_1}\right)^* \tag{3.12a}$$

$$T = \frac{4\,\mathrm{Re}(y_0)\mathrm{Re}(y_1)}{(y_0 + y_1)(y_0 + y_1)^*} = \frac{4n_0 n_1}{(N_0 + N_1)(N_0 + N_1)^*} \tag{3.12b}$$

The reflectance of an assembly of thin films, sketched in Figure 3.2, is calculated through the concept of optical admittance. By replacing the multi-layer by a single surface, the input optical admittance Y is given as:

$$Y = C/B \tag{3.13}$$

where

$$\begin{bmatrix} B \\ C \end{bmatrix} = \prod_{r=1}^{q} \begin{bmatrix} \cos\delta_r & (i\sin\delta_r)/\eta_r \\ i\eta_r \sin\delta_r & \cos\delta_r \end{bmatrix} \cdot \begin{bmatrix} 1 \\ \eta_m \end{bmatrix} \tag{3.14}$$

is the characteristic matrix of q layers. It is simply the product of the individual matrices taken in the correct order, with:

$$\delta_r = 2\pi N_r d_r \cos\theta_r / \lambda$$

$\eta_r = \mathcal{Y} N_r \cos\theta_r$ for s-polarization (*TE*)

$\eta_r = \mathcal{Y} N_r / \cos\theta_r$ for p-polarization (*TM*)

where suffix m denotes the substrate or exit medium.

$\eta_m = \mathcal{Y} N_m \cos\theta_m$ for s-polarization (*TE*)

$\eta_m = \mathcal{Y} N_m / \cos\theta_m$ for p-polarization (*TM*)

Therefore, the amplitude reflection coefficient and the reflectance are:

$$\rho = \frac{\eta_0 - Y}{\eta_0 + Y}, \qquad R = \left(\frac{\eta_0 - Y}{\eta_0 + Y}\right)\left(\frac{\eta_0 - Y}{\eta_0 + Y}\right)^* \tag{3.15}$$

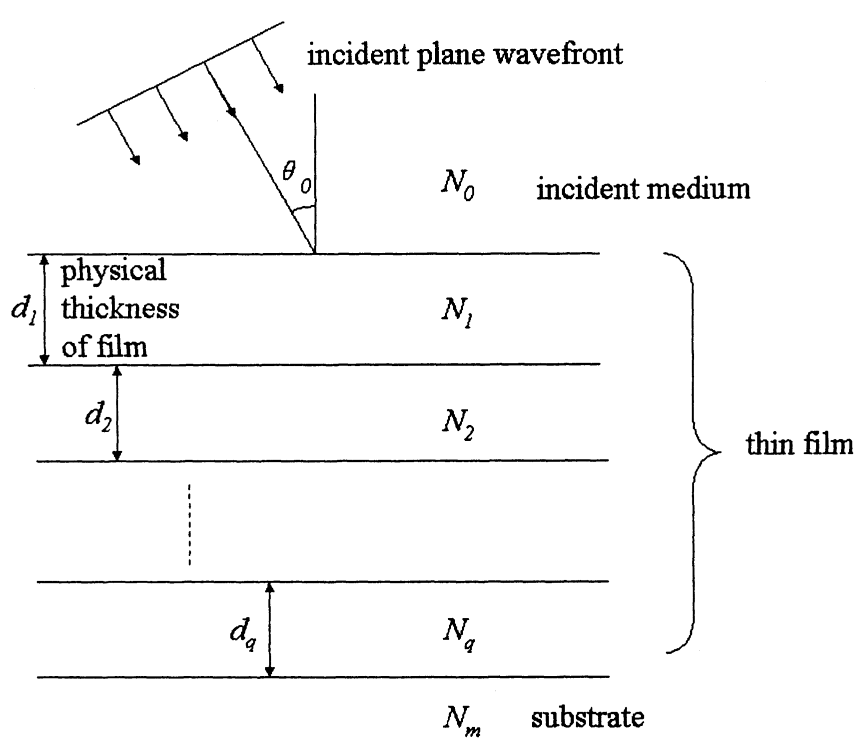

Figure 3.2 Plane wave incident on an assembly of thin films

The expressions (3.13), (3.14) and (3.15) are of prime importance in optical thin-film design and form the basis of the calculations in this work.

3.3 DESIGN OF BROAD-BAND MULTI-LAYER ANTIREFLECTION COATINGS

AR coatings were the principal objective of much of the early work in thin-film optics. Of all the possible applications, it has had the greatest impact on technical optics.

Conventional AR coatings originated from a single-layer quarter-wavelength film with a refractive index equal to the square root of that of the substrate. The disadvantage of the single-layer AR coating, as far as the design is concerned, is the limited number of adjustable parameters. The refractive index, or optical admittance, of the layer is uniquely determined as $\eta_1 = (\eta_0 \eta_m)^{1/2}$. There is no room for manoeuvre in the design of a single-layer coating. In practice, the refractive index is not a parameter which can be varied at will. Materials suitable for use as thin films are limited in number and the designer has to use what is available. There is also a limitation that the single-layer AR coating can give zero reflectance at one wavelength only and low reflectance only over a narrow region. Another design concern is that the tolerances for achieving a low reflectance with single-layer coating are quite small. To achieve a facet reflectance of 10^{-4} requires film index and thickness tolerances of ± 0.01 and $\pm 1\,\text{nm}$, respectively.

A more rewarding approach, therefore, is to use more layers, specifying obtainable refractive indices for all layers at the start, and to achieve a broader region of low reflectance by varying the optical thickness of each layer. Various multi-layer AR coatings have been reported in the past years: stepwise-graded-index multi-layer coatings [30], double-layer coatings [31], and triple-layer coatings for semiconductor lasers [32].

There is no general systematic method for the design of multi-layer AR coatings. Trial and error, assisted by accurate computer calculations, are frequently employed [33]. In this work, all the performances have been computed by application of the matrix method discussed in previous section. In all cases, the materials are considered to be completely transparent.

The vast majority of AR coatings are required for matching an optical element to air. Air has an index of around 1.0003 at standard temperature and pressure which, for practical purposes, can be considered as unity.

To obtain a multi-layer AR coating model, the design was started with the standard design procedure of multi-layer coatings, based on the optical admittance matching technique [34,35]. The reflectivity of an assembly of thin films is calculated through the concept of the optical admittance, expressions (3.13) and (3.14). Coating materials should be determined by the matching condition taking into consideration their optical properties, fabrication simplicity, stability, and cost. For the dielectric materials used for the AR coatings in this work, the extinction coefficient is virtually zero in the visible and near infrared ranges so that the absorptivity can be ignored in the coating designs (this will be discussed in detail in section 4.3).

If the materials are considered to be non-absorptive, with no dispersion, at normal incidence, the reflectivity and the transmittivity are:

$$R = \left(\frac{n_0 B - C}{n_0 B + C}\right) \cdot \left(\frac{n_0 B - C}{n_0 B + C}\right)^* = \left|\frac{Y - n_0}{Y + n_0}\right|^2 \tag{3.16}$$

$$T = 1 - R \tag{3.17}$$

The condition for obtaining zero reflectivity is that the optical admittance Y is equal to n_0 (optical admittance matching), of which the real and imaginary parts must equate separately

$$\begin{cases} \mathrm{Re}(Y - n_0) = 0 \\ \mathrm{Im}(Y - n_0) = 0 \end{cases} \tag{3.18}$$

Instead of optical admittance matching, the design algorithm in this work was based on its detuning. By introducing a detuning factor Δ, a wider range of design parameters could be tried by relaxing the optical admittance matching condition, i.e.,

$$\begin{cases} \mathrm{Re}(Y - n_0) \le \Delta \\ \mathrm{Im}(Y - n_0) \le \Delta \end{cases} \tag{3.19}$$

Optical admittance matching, given in Eq(3.18), implies that the minimum reflectivity is at the center wavelength, and it is zero. The detuning expression (3.19) gives certain ranges of solutions surrounding the matched point. The AR coating design with the broadest bandwidth for a given system exists at one of those solutions. Therefore, a broad-band AR coating design typically has multiple solutions. Which solution should be chosen is determined by means of deposition simplicity and stability, as well as the obtainable refractive indices and physical thickness of the dielectric materials. The design procedure for multi-layer AR coatings is shown in Figure 3.3. The operation of the ECR-PECVD system, and refractive index and thickness control by *in situ* ellipsometry will be discussed in next chapter.

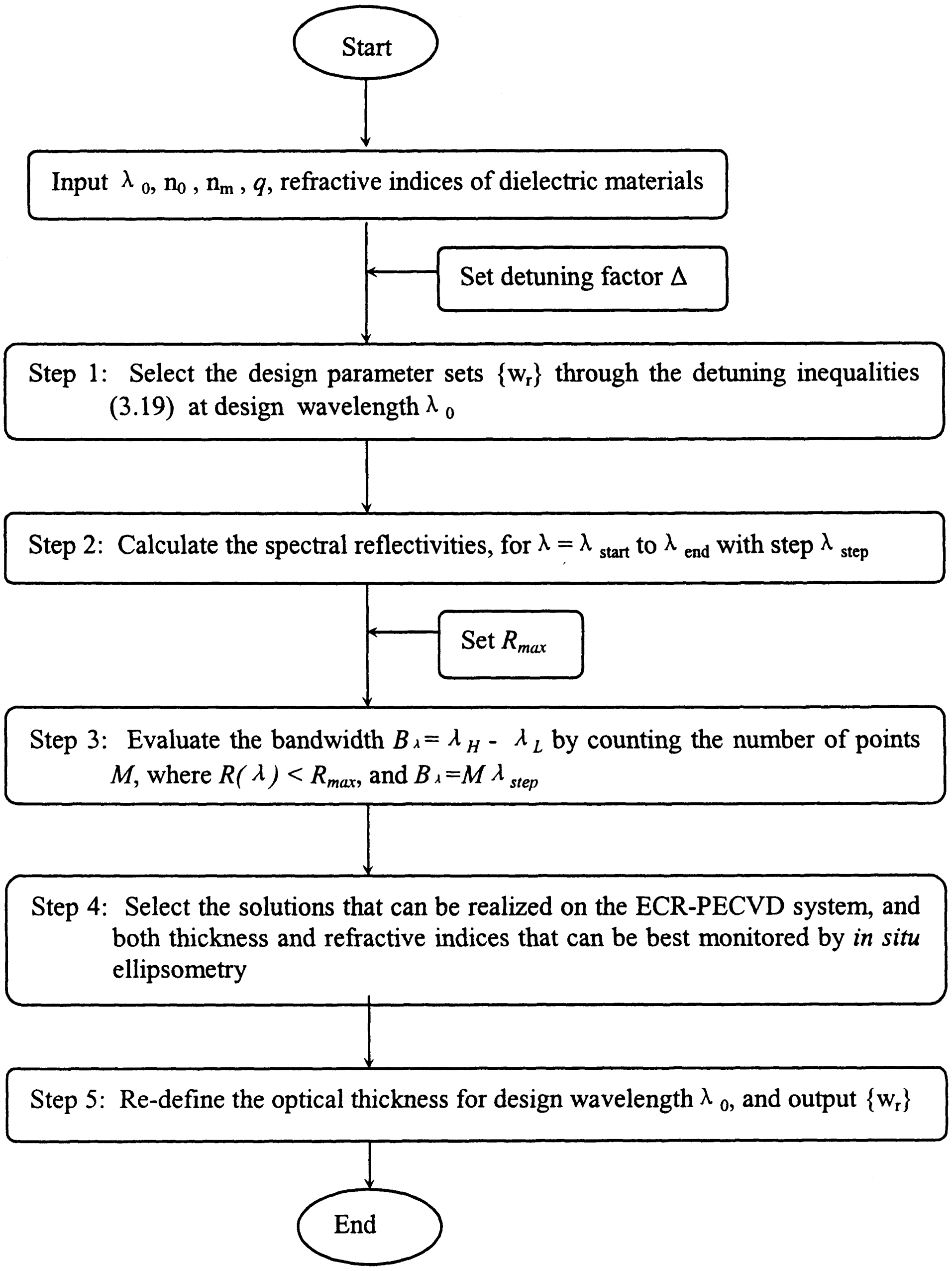

Figure 3.3 Flowchart of AR coating design

3.4 ANTIREFLECTION COATING MODELS USED IN THIS WORK

Following the discussions above, the design parameters for double-layer and triple-layer AR coatings were derived and are listed in Table 3.1. The materials used in the designs are SiO_2, Si_3N_4, a:Si, and SiO_xN_y. The optical properties of these materials deposited by the ECR-PECVD technique will be discussed in Chapter 4.

The diode lasers are ridge waveguide InGaAsP/InP MQW lasers of different emission wavelengths. The determination of the effective refractive index of the diode lasers is described in Chapter 2. The bandwidth for reflectivities less than 10^{-3} and 10^{-4} were calculated, and refinement factors (optical thickness divided by quarter wavelength) were given for each layer for ease of calculation.

Table 3.1(a) Model 1: double-layer AR coating using SiO_2/Si_3N_4

λ =1660nm

Layer	refractive index	thickness (nm)	refinement factor
Air	1.000		
SiO_2	1.444	133.37	0.4641
Si_3N_4	1.950	159.31	0.7486
Laser	3.228		
bandwidth(nm) (reflectivity<10^{-3})	122		
bandwidth(nm) (reflectivity<10^{-4})	38		

Table 3.1(b) Model 2: double-layer AR coating using SiO_2/Si_3N_4

λ =1550nm

Layer	refractive index	thickness (nm)	refinement factor
Air	1.000		
SiO_2	1.444	126.48	0.4713
Si_3N_4	1.950	147.91	0.7443
Laser	3.212		
bandwidth(nm) (reflectivity<10^{-3})	115		
bandwidth(nm) (reflectivity<10^{-4})	36		

Table 3.1(c) Model 3: triple-layer AR coating using $SiO_2/Si_3N_4/Si$

λ =1550nm

Layer	refractive index	thickness (nm)	refinement factor
Air	1.000		
SiO_2	1.444	122.96	0.4582
Si_3N_4	1.950	153.31	0.7715
Si	3.450	16.75	0.1490
Laser	3.210		
bandwidth(nm) (reflectivity<10^{-3})	113		
bandwidth(nm) (reflectivity<10^{-4})	35		

Table 3.1(d) Model 4: triple-layer AR coating using $SiO_2/Si/SiO_xN_y$

λ =1550nm

Layer	refractive index	thickness (nm)	refinement factor
Air	1.000		
SiO_2	1.444	296.21	1.1074
Si	3.450	44.19	0.3947
SiO_xN_y	1.570	52.84	0.2148
Laser	3.210		
bandwidth(nm) (reflectivity<10^{-3})	395		
bandwidth(nm) (reflectivity<10^{-4})	175		

3.5 SUMMARY

In this chapter, a design procedure of broad-band multi-layer AR coatings was proposed by introducing the optical admittance detuning concept. SiO_2, Si_3N_4, a:Si, and SiO_xN_y were primarily used in the designs as coating materials, giving a wide range of refractive indices from 1.444 to 3.450.

As pointed out in section 3.3, the design of AR coatings is typically a multi-solution problem. The best-optimized design is not unique, but is dependent on the required upper limit of reflectivity (R_{max}) for a desired application.

There are tremendous designs with low reflectivity and broadest bandwidth in various published resources, often time few design details are published. Meanwhile, some commercial software, such as TFCalc [36], can always provide a suitable solution, but it seems lacking in flexibility. And the user never knows how the solutions work out.

The results obtained here only represent some of the possible solutions for broad-band AR coatings, and were made applicable for the ECR-PECVD system only (which will be discussed next). Using dielectric materials other than the materials being used in this work, such as TiO_2, will end up with different solutions by different deposition methods (i.e., electron beam evaporation).

CHAPTER 4

FABRICATION OF ANTIREFLECTION COATINGS

4.1 INTRODUCTION

Dielectric thin films are used for a wide range of applications in compound semiconductor (GaAs, InP) devices including diffusion and ion implantation masks, intermetal isolation layers, passivation films, optical coatings, and waveguides for both electronic and optoelectronic applications. Dielectric films such as SiO_2, Si_3N_4, SiO_xN_y, Al_2O_3, AlN, TiO_2 and ZrO_2, are commonly used and have been deposited on GaAs and InP by a variety of techniques including chemical vapor deposition (CVD), electron beam evaporation, and various ion-assisted deposition processes [37].

Independent of specific device structures, four principal requirements for the deposition of thin films for optoelectronics are: low temperature deposition, control of refractive index and thickness, control of film stress, and low facet damage. To this end, electron cyclotron resonance (ECR) plasma sources have been developed for low pressure, low temperature and, potentially, low damage deposition for dielectric thin films. The potential advantages of ECR plasma CVD have had significant impact on III-V semiconductor device fabication.

In this chapter, the fabrication of AR coatings designed according to Chapter 3 is presented. The coating structures were deposited by electron cyclotron resonance plasma enhanced chemical vapor deposition (ECR-PECVD). The coating materials were silicon dioxide (SiO_2), silicon nitride (Si_3N_4), silicon oxynitride (SiO_xN_y) and amorphous silicon (a:Si), with refractive indices varying from 1.444 to 3.450 around 1.5 μm. A run to run reproducibility in the refractive index of 0.008 and a thickness control of $\pm 10Å$ [38] were obtained using *in situ* ellipsometry for optical monitoring.

4.2 ECR-PECVD SYSTEM

In an ECR-PECVD system, one uses a plasma to crack the precursor gas to deposit the desired materials onto a substrate. The primary advantage of an ECR-PECVD system over other deposition systems for semiconductor applications is that the velocity of the ions and reactive species impinging on the sample can be controlled by the magnet design such that the energies are small enough to avoid damaging the sample surfaces [39]. This is an important design and experimental consideration for diode lasers based on InGaAsP/InP materials, since these materials are particularly sensitive to facet damage and elevated temperatures, where excessive heating can result in the loss of group V elements. Additionally, if point defects are introduced through ion bombardment, these defects could result in local centers of heating which could cause deterioration of the laser performance and eventually lead to premature failure [40].

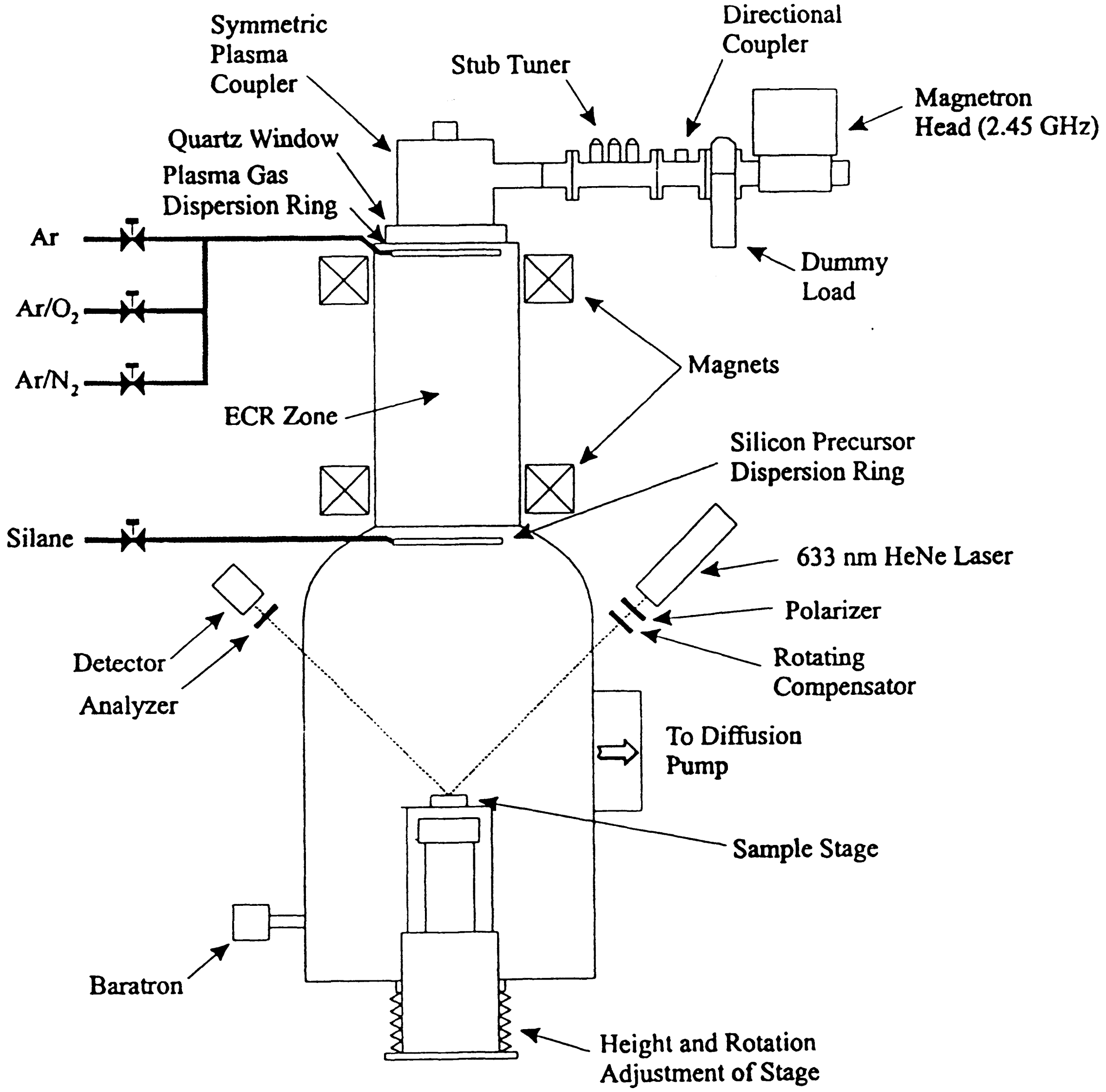

Figure 4.1 ECR-PECVD system

A schematic diagram of the ECR-PECVD system is shown in Figure 4.1. Microwave power generated by the magnetron head is introduced into the top of the plasma generation chamber through a quartz window. Stub tuners, positioned along the waveguide, are used to impedance match the waveguide system to optimize the power coupled into the plasma by reducing the reflected power.

Two large electromagnets are positioned around the upper half of the deposition chamber. The plasma gases (Ar, O_2 and N_2) are introduced through a dispersion ring at the top of the deposition chamber. When the magnets and microwave power are on, the electrons in the plasma experience a Lorentz force proportional to the electric and magnetic fields applied:

$$\mathbf{F} = q(\mathbf{E}+\mathbf{v}\times\mathbf{B}) \tag{4.1}$$

The magnetic component causes the electrons to follow a helical path with a cyclotron frequency of

$$\omega_c = eB/m_e \tag{4.2}$$

and a radius defined by conservation of energy. Here, e is the electron charge, B the appropriate magnetic field strength in Gauss, and m_e the electron mass. By tuning the magnetic field so that the cyclotron frequency matches the microwave frequency, a resonant condition exists where the electrons continuously gain energy from the electric field. The region where this holds is referred to as the ECR zone. As the electrons gain energy, the radii of their helixes increase, thereby increasing the probability of collisions with other particles in the plasma. Eventually, a state of dynamic equilibrium is reached where there is a balance of the energy gained from the electric field and the energy lost through collisions. In this work, the microwave frequency used is 2.45 GHz, so the corresponding magnetic field strength required to satisfy the resonant condition is 875 G.

The silicon precursor is introduced through a dispersion ring located below the lower magnet. Ar, O, and N ions leaving the plasma collide with the precursor gas molecules, breaking them into various radical species which may react with one another at the sample surface, forming various thin films. The path of the silicon precursor from the dispersion ring to the sample surface is quite direct, involving only a small number of activating collisions. A carefully-designed gas dispersion ring ensured that a reasonable film uniformity can be obtained [38]. Waste products are pumped out from the deposition system by a diffusion pump.

For all the depositions performed in this work, the pressure in the chamber was maintained at 2.4 mTorr, the currents in the upper and lower magnets were set to 180A and 115A, respectively, the substrate temperature was generally kept at 120^0C, and the microwave power was 500W. Typically, depositions are carried out at reflected powers less than 5% of the transmitted power. The total gas flow rate during the deposition was generally between 30 and 60 sccm, depending on the gas mixtures. Reliable control of the film refractive index was only achieved when the base pressure of the chamber was kept below 10^{-7} Torr, after baking the chamber walls a pressure of 5×10^{-8} Torr was obtained.

The silicon precursor used in this work is silane (SiH_4). Silane is the most popular source of silicon in plasma enhanced depositions, and is commonly used in industry. This material is pyrophoric, reacting violently with oxygen in the air upon contact; however, it is the most simple silicon compound available. The reaction kinetics of SiH_4 have been studied for many years, and there is a tremendous amount of literature available [41]. Most studies concluded that the SiH_4 molecule undergoes abstraction processes in the gas phase to produce silylene (SiH_2) , and silyl (SiH_3), along with hydrogen gas molecules. The silicon radicals then act as precursors to film deposition and undergo a heterogeneous reaction at the deposited film surface to become incorporated into the film with the release of more hydrogen.

During the past years, extensive work has also been done on using tris(dimethylamino) silane (TDAS, $((CH_3)_2N)_3SiH$) as the silicon precursor because it is a safer alternative [42]. Due to the nitrogen content in TDAS, however, it is not suitable for depositing the highest index films, such as a:Si. Therefore, in this work SiH_4 was used for the deposition of films of the type SiO_xN_y, and a:Si, providing a wider range of refractive indices than TDAS, thus allowing the realization of more sophisticated interference filter designs.

Before deposition, the sample was mounted on a sample holder and transported horizontally into the deposition chamber via a load-lock system (not shown in Figure 4.1). The sample holder was then placed on a heated stage in the deposition chamber. The heater beneath the stage was set to 350^{0}C, corresponding to 120^{0}C of sample temperature [38].

Laser bars were mounted as shown in Figure 4.2. The laser bars were held in place by weak horizontal pressure from two pieces of silicon wafer mounted on the sample holder. One of the silicon wafers can be used as a witness wafer during the deposition.

As shown in Figure 4.2, the two silicon wafers are not of equal thickness. The wafer close to the active region of the laser usually has a smaller thickness compared to the cavity length of the diode laser; while the wafer close to laser substrate usually has much larger thickness. By mounting the laser bar like this, the electrical contacts of the diode lasers can be satisfactorily masked during the deposition, meanwhile avoiding possible shadowing effects from the silicon wafer of larger thickness.

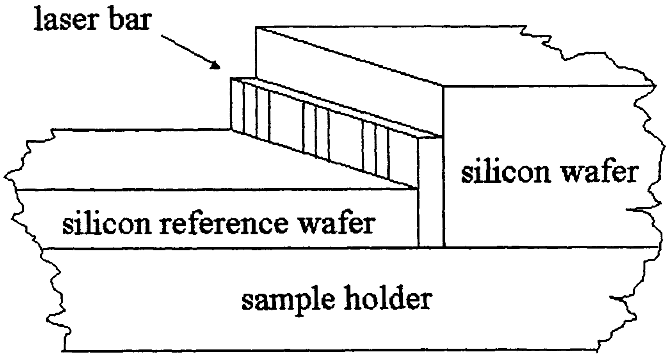

Figure 4.2 A schematic diagram of a laser bar mounted on the sample holder for optical coating

4.3 OPTICAL PROPERTIES OF SiO_2 / Si_3N_4 / SiO_xN_y / a:Si

SiO_2, Si_3N_4, SiO_xN_y and a:Si are extremely important materials in many areas of semiconductor device fabrication. These materials have been studied for more than two decades. In this section, optical properties of these materials from various published sources are discussed and summarized in Table 4.1.

Table 4.1 Optical properties of SiO_2/Si_3N_4/a:Si/SiO_xN_y

Materials	Refractive Index	Region of Transparency
Silicon Dioxide (SiO_2)	1.457@632.8nm 1.444@1.55 micron	200 nm - 8 micron
Silicon Oxynitride (SiO_xN_y)	1.462 ~ 2.0 @632.8nm	900nm-2600nm
Silicon Nitride (Si_3N_4)	2.015@632.8nm 1.998@1.24 micron 1.950@1.55 micron	290 nm - 10 micron
Amorphous Silicon (a:Si)	~ 3.4 in IR	1.1 micron- 14 micron

4.3.1 SiO_2 and Si_3N_4

The optical properties of SiO_2 and Si_3N_4 can be found in the literatures [43,44,45,46]. Usually, their optical properties are determined either from spectrophotometric (reflectance *R* and/or transmittance *T*) or ellipsometric measurements, among which variable angle spectroscopic ellipsometry (SE) combined with *R* and *T* measurements appears to be most powerful. The refractive indices of SiO_2 and Si_3N_4 being used in this work were taken from the above references. Both materials are transparent in the visible and near infrared regions.

4.3.2 a:Si

Amorphous silicon (a:Si) films were deposited using an Ar/SiH_4 gas mixture. The extinction coefficient of the complex refractive index was found to be less than 3×10^{-4} indicating nonabsorbing a:Si films [40]. The refractive index in the 1310nm to 1550nm region was reported to be around 3.4 [47,48]. Some lower reported values of the refractive index for a:Si are likely due to some hydrogen bonding in the a:Si structure [40,48].

4.3.3 SiO_xN_y

There has been a growing interest in SiO_xN_y films in the past years because of their transparency in the visible and near infrared regions, and their wide refractive index range, theoretically varying from the refractive index of

SiO_2 (1.457 at 632.8nm) to the refractive index of Si_3N_4 (2.015 at 632.8nm). SiO_xN_y is considered as the best material for graded refractive index films for applications in optical devices, and particularly in optical filters [49].

The optical properties of SiO_xN_y were studied and reported a number of years ago [50,51]. Generally, the optical behavior of a homogeneous layer of SiO_xN_y can be described by using the Bruggeman effective medium approximation (EMA) [52,53]. The EMA considers the SiO_xN_y film as an isotropic physical mixture of two phases, SiO_2 and Si_3N_4 , homogenous on the scale of the wavelength. The index of the mixture could be calculated from the volume fractions of its components, assuming that these retain their intrinsic optical properties. This approximation provides a simple description of the SiO_xN_y dispersion law when the dispersion laws of SiO_2 and Si_3N_4 are known.

Bruggeman EMA can be a practical way for roughly modeling *n* and *k* of SiO_xN_y , but it cannot provide precise information relative to the composition and structure. Actually, SiO_xN_y is not a simple physical mixture of SiO_2 and Si_3N_4 [50,51]. The limitations in the use of the EMA approaches are due to following concerns:

i) hydrogen incorporated in the films reduces *n*, which is difficult to account for in the EMA model

ii) films deposited at high ion energy or substrate temperatures represent solid solutions at the atomic level, containing O-Si-N bonds, hence no SiO_2 and Si_3N_4 domains can be distinguished

iii) the optical characteristics may be shrouded by the presence of pores (possibly filled with water vapor), which result in lower *n*

Bulkin *et al.* [54] reported the wavelength dependencies of the refractive index and extinction coefficient of SiO_xN_y films deposited by ECR-PECVD from O_2/Ar, N_2/Ar and SiH_4/Ar mixtures, and investigated the optical properties of the films by means of transmission spectroscopy in the wavelength range 200nm ~ 2600nm. They found all layers to be transparent in the 900nm ~ 2600nm region, but there is a shift of the absorption edge towards shorter wavelengths. The real part of the refractive index is approximately wavelength independent in certain wavelength regions (these regions depend on the deposition conditions and gas mixtures ratios), which cover the 1.3 μm and 1.5 μm windows. Tompkins *et al.* [55] analyzed silicon oxynitrides with spectroscopic ellipsometry and Auger spectroscopy, comparing them with the analyses by Rutherford backscattering spectrometry (RBS) and Fourier transform infrared spectroscopy (FTIR), and reached similar results.

4.4 FILM THICKNESS AND REFRACTIVE INDEX CONTROL BY *in situ* ELLIPSOMETRY

Ellipsometry is an old, but still very popular and powerful optical technique for studying surfaces and thin films. The fundamental principles of the technique are well known. The following is a brief review of salient features that are directly applicable to ellipsometry.

4.4.1 Theoretical Aspects

Figure 4.3 is an illustration of reflections and transmissions at multiple interfaces.

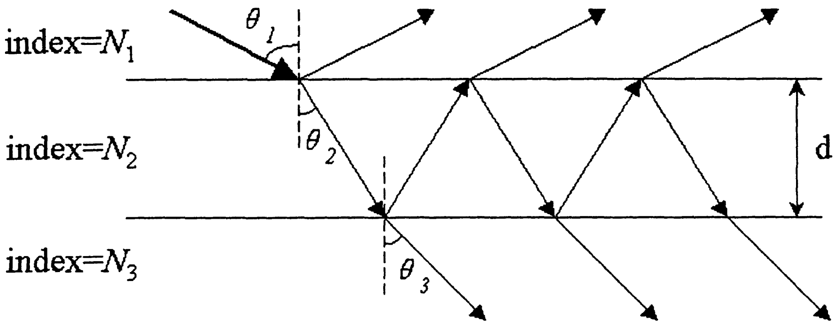

Figure 4.3 Reflections and transmissions at multiple interfaces

The resultant reflected wave returning to medium 1 is made up of the light reflected directly from the first interface plus all of the transmissions from the light approaching the first interface from medium 2. Each successive transmission back into medium 1 is smaller in intensity. The addition of this infinite series of partial waves leads to the resultant wave. The ratio of the amplitude of the resultant reflected wave to the amplitude of the incident wave can be given by the total reflection coefficients [56]:

$$R^p = \frac{r_{12}^p + r_{23}^p \exp(-i2\beta)}{1 + r_{12}^p r_{23}^p \exp(-i2\beta)} \tag{4.3a}$$

$$R^s = \frac{r_{12}^s + r_{23}^s \exp(-i2\beta)}{1 + r_{12}^s r_{23}^s \exp(-i2\beta)} \tag{4.3b}$$

where p and s refer to waves parallel and perpendicular to the plane of incidence, respectively. Subscript "12" (or "23") denotes that the Fresnel reflection coefficient is for the interface between medium 1 and medium 2 (or medium 2 and 3). The Fresnel reflection coefficients for the interface between medium 1 and medium 2 are given by [57a]:

$$r_{12}^p = \frac{N_2 \cos\theta_1 - N_1 \cos\theta_2}{N_2 \cos\theta_1 + N_1 \cos\theta_2} \tag{4.4a}$$

$$r_{12}^s = \frac{N_1 \cos\theta_1 - N_2 \cos\theta_2}{N_1 \cos\theta_1 + N_2 \cos\theta_2} \tag{4.4a}$$

where, N_1 and N_2 are the complex refractive indices of medium 1 and medium 2, respectively. Similar coefficients can be derived for the interface between medium 2 and medium 3. β in Eq(4.3) is the film phase thickness and is given by [56]:

$$\beta = 2\pi\left(\frac{d}{\lambda}\right)N_2 \cos\theta_2 \tag{4.5}$$

where d is the film thickness. Therefore, the reflectance $\mathfrak{R}$ is given by:

$$\mathfrak{R}^P = \left|R^p\right|^2 \quad \text{and} \quad \mathfrak{R}^S = \left|R^s\right|^2 \tag{4.6}$$

If δ_1 denotes the phase difference between p-polarization and s-polarization of the incoming wave, and δ_2 that for the outgoing wave, the parameter Δ, called delta or often abbreviated "Del", is defined as:

$$\Delta = \delta_1 - \delta_2 \tag{4.7}$$

Del, then, is the change in phase difference that occurs upon reflection and its value can be from zero to 360^0.

Without regard to phase, the amplitude of both perpendicular and parallel components may change upon reflection. $|R^p|$ and $|R^s|$ from Eq(4.3) are the ratios of the outgoing wave amplitude to the incoming wave amplitude for the parallel and perpendicular components, respectively. The quantity Psi, Ψ, is defined as:

$$\tan\Psi = \frac{|R^p|}{|R^s|} \tag{4.8}$$

Ψ, then, is the angle whose tangent is the ratio of the magnitudes of the total reflection coefficients. The value of Ψ can be between zero and 90^0. Therefore the fundamental equation of ellipsometry is:

$$\rho = \tan\Psi \cdot e^{j\Delta} \qquad \text{or} \qquad \tan\Psi \cdot e^{j\Delta} = \frac{R^p}{R^s} \tag{4.9}$$

where the complex quantity ρ (rho) is the complex ratio of the total reflection coefficients, Δ and Ψ are the quantities measured by an ellipsometer. The information about the sample in question is contained in the total reflection coefficients, or R^p and R^s.

It should be noted that assuming the instrument is operating properly, the quantities Δ and Ψ which are measured are always correct. Whether the calculated sample parameters, such as thickness and refractive index, are correct or not depends on whether the assumed model is correct. Therefore, the reliability of the calculated properties is only as good as the assumed model. If an improper model is assumed, although the values of Δ and Ψ are correct, the calculated quantities may well be meaningless.

4.4.2 Ellipsometric Monitoring

A He-Ne laser operating at a wavelength of 632.8nm is used as the light source in a rotating-compensator Fourier ellipsometer, *Model i1000, Rudolph Research Systems*, shown in Figure 4.4. It consists of a polarizer and an analyzer, both set at an azimuth of 45^0, a rotating compensator, a detector, and the sample under investigation. Careful calibration for the ellipsometer is required before the operation [58].

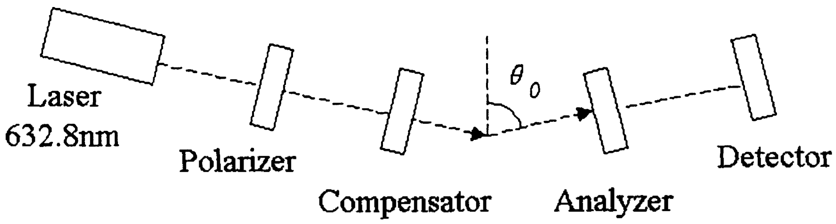

Figure 4.4 Schematic diagram of the rotating-compensator Fourier ellipsometer

In the measurement process, the intensity at the detector is:

$$I(C) = A_0 + A_2 \cos 2C + B_2 \sin 2C + A_4 \cos 4C + B_4 \sin 4C \qquad (4.10)$$

where C is the angle of the fast axis azimuth of the compensator crystal relative to the plane of incidence of the sample. A_i, B_i are Fourier coefficients, and are determined by a calibration process [58].

Three reference wafers of known refractive index and thickness were measured with the present ellipsometer. From this, three sets of Δ and Ψ were obtained for a total of six parameters. These six parameters were used to calculate the actual ellipsometer angle of incidence (AOI) and the window optical properties. At the time of the thin-film depositions and optical measurments, the AOI of the ellipsometer was 75.823^0, and the complex refractive index of the substrate assumed in the model was $3.858 - i0.018$.

For a number of dielectric materials deposited by ECR-PECVD, the extinction coefficient is virtually zero in the visible and near infrared regions. Using Eq(4.3)-Eq(4.9), the expected values of Δ and Ψ can be calculated, and plotted as so called "Del/Psi trajectories", shown in Figure 4.5. Here the "Del/Psi trajectories" refers to the changes in the values of Del and Psi as a function of film thickness and refractive index.

Figure 4.5(a) shows essentially the complete trajectories for the films with refractive indices for 1.46, 1.57, 2.0 on single crystal silicon. These indices are typical of SiO_2, SiO_xN_y, and Si_3N_4 , respectively. SiO_xN_y of refractive index of 1.57 was previously used in the triple-layer AR coating design shown in Table

3.1(d). Although two of these trajectories appear to be discontinuous, one should recall that for a fixed value of Ψ, the value of $\Delta=0$ and $\Delta=360$ are the same.

An unknown thickness and refractive index of a thin film deposited on a silicon sample can be determined by comparing the measured values of Δ and Ψ with the curves shown in Figure 4.5(a). Practically, the curve on which the measured point (Δ,Ψ) falls determines the refractive index of the thin film. The position on that curve determines the film thickness. By changing the refractive index of the thin film and/or the film thickness, a different set of Δ and Ψ values would be obtained.

In the ECR-PECVED system, when beginning to deposit an optical thin film onto the substrate, the Del/Psi point begins to move down and to the right, tracing out the trajectory. By assigning the refractive index of the thin film to a particular value in the control program, e.g., $n = 1.57$ for SiO_xN_y, the film thickness will follow a particular trajectory. Other values of refractive index would give different trajectories. Therefore, one can control the film thickness precisely during the depositions. This is extremely helpful especially when all the trajectories are not well-separated, e.g., at the beginning of the deposition, or when depositing optical films less than 50nm thick. This situation is illustrated in Figure 4.5(b). At this point, a modified *Turbo C++ (Ver.3.0)* program was used, which could set the refractive index of the thin film to the design value before the deposition, and then one could monitor the growing film thickness precisely during the deposition. In practice, to determine the refractive index of SiO_xN_y film (or to figure out the gas mixture ratio for the required refractive index), one or two trial runs could be done, using silicon wafers onto which SiO_xN_y films of about 100nm thickness were deposited. For larger thickness, the trajectory in Figure 4.5(a) simply retraces the same path.

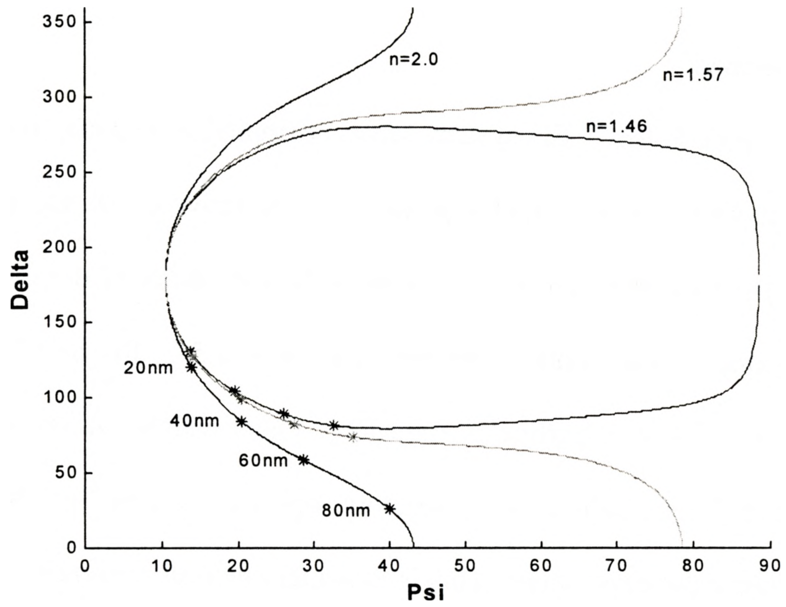

Figure 4.5(a) The Del/Psi trajectories for films with several different refractive indices, angle of incidence (AOI) = 75.823^0.

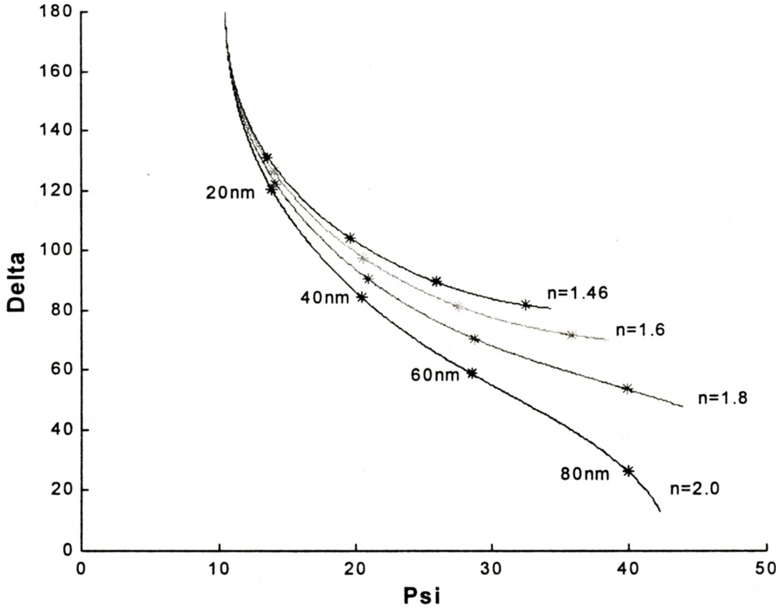

Figure 4.5(b) Close look at the beginning of the depositions when all the trajectories are not well-separated, AOI = 75.823^0.

4.5 FACET REFLECTIVITY

There are many different methods for measuring the reflectivity of AR-coated facets. Some of the commonly used methods are presented below.

The first method is a simple approach, but it can be used only for devices with one coated facet and only when the beams from both facets are unobstructed. After coating, the laser is operated above its new, higher threshold current and the *L-I* curves from both facets are measured. The unknown reflectivity of the coated facet is related to the assumed known Fresnel reflectance of the uncoated facet by [59]:

$$\frac{\eta_c}{\eta_u} = \sqrt{\left(\frac{R_u}{R_c}\right)\frac{(1-R_c)}{(1-R_u)}} \tag{4.11}$$

where η_u and η_c are the slope efficiencies for the uncoated and coated facets, respectively. Obviously, this method only determines the facet reflectance at the emission wavelength of the solitary diode laser.

The second method [60] can be applied to gain media with AR coatings on one or both facets, and it does not require an unobstructed beam from either facet. It relates a change in the round-trip amplification factor to a change in the modulation index of the emission spectrum. The magnitude of the round-trip amplification factor is given by

$$|a| = \sqrt{R_{f1}R_{f2}}\exp[(g-\alpha_{\text{int}})L_{\text{int}}] \tag{4.12}$$

For an uncoated laser, $R_{f1} = R_{f2} = R_u$, where R_u is the Fresnel reflectance of an uncoated facet. In order to conserve energy, $|a| \leq 1$, and at laser threshold $|a| \approx 1$. After coating, the value of $|a|$ at the same current and wavelength is reduced to

$$|a|^2 = \frac{R_{f1}R_{f2}}{R_u^2} \tag{4.13}$$

The modulation index *m* of the sub-threshold emission is given by

$$m = \frac{P_{\max} - P_{\min}}{P_{\max} + P_{\min}} \tag{4.14}$$

where $P_{\max}$ and $P_{\min}$ are, respectively, the local maximum and minimum at the peak of the emission spectrum. When the coated device is driven at the original uncoated-laser threshold current, $|a|$ is related to m by

$$m = \frac{2|a|}{1+|a|^2} \tag{4.15}$$

This method, like the previous one, is strictly accurate only at the original oscillation wavelength of the solitary diode laser. At other wavelengths the gain is lower, and this method tends to underestimate the reflectance. Furthermore, when both facets have been coated, it is often difficult to measure m, and the method only gives the product of the two coating reflectivities.

The third method is by means of analyzing the amplified spontaneous emission (ASE) spectra. Currently, two techniques are available to evaluate the reflectivity of an AR-coated diode laser facet, and it is the sum/min method (described in the following) that was utilized in this work.

When a diode laser is operated below threshold, its broad spectral profile is modulated by a series of peaks and valleys corresponding to the Fabry-Perot cavity modes generated by the laser facets. The modulation depth of these structures is a function of the facet reflectivities of the laser under study. The steady-state output intensity of the optical frequency $I^{\pm}(\nu)$ from the left (-) or right (+) end of a laser is [61]:

$$I^{\pm}(\nu) = \frac{B(1 + R_{\mp}G)(1 - R_{\pm})}{(1 + RG)^2 - 4RG\sin^2\theta} \tag{4.16}$$

where $R_{\pm}$ are the reflectivities of the mirrors forming the resonator, G is the single-pass intensity gain, B is the total amount of spontaneous light of frequency ν coupled into the laser mode, and $R^2 = R_+R_-$, $\theta = 2\pi\, l\nu/c$ where $c/2l$ is the free spectral range of the resonator.

The conventional Hakki and Paoli method [62] (so called HP method or max/min method) for evaluation of the laser facet reflectivity relies on the measurements of oscillatory ASE spectra both before and after AR coating at the same injection current level [23,63]. Since the gain and the spontaneous emission spectra are common, whereas only the reflectivity is changed, the difference in peak-to-valley ratio will give a direct estimate of the reflectivity after the coating. This approach involves the measurement of the maxima and minima of the Fabry-Perot spectrum, and the net gain is given by:

$$G(\lambda) = \frac{1}{L}\ln\left(\frac{r^{1/2} - 1}{r^{1/2} + 1}\right) + \frac{1}{L}\ln\left(\frac{1}{R}\right) \tag{4.17}$$

where r is the peak to valley ratio of the i^{th} mode. When rearranging Eq(4.16), r is found to be:

$$r = \frac{(1 + RG)^2}{(1 - RG)^2} \tag{4.18}$$

or isolating the RG product,

$$RG = \frac{\sqrt{r}-1}{\sqrt{r}+1} \tag{4.19}$$

Therefore, the product of the facet reflectivities and the gain can be determined for each mode by measuring the peak-to-valley ratio for the Fabry-Perot modulations in the laser's emission spectrum under threshold.

One fundamental requirement of Hakki and Paoli's method is a high wavelength resolution provided by the measurement system. Practically, one cannot measure the peak to valley ratio very accurately, because the measured signal represents the true laser spectrum convolved with the instrument response function, thereby reducing the recorded modulation depth.

To overcome this difficulty, an alternative approach was proposed by Cassidy [61], which made use of the integral in Eq(4.16) over the free spectral range, together with the minimum of each individual mode. The net gain is thus given by:

$$G(\lambda) = \frac{1}{L}\ln\left(\frac{p-1}{p+1}\right) + \frac{1}{L}\ln\left(\frac{1}{R}\right) \tag{4.20}$$

where p is the ratio of the integral over one mode to the mode minimum, $p = p'2l/c$, and

$$p' = \frac{c}{2l}\frac{1+RG}{1-RG} \tag{4.21}$$

Isolating the RG product gives:

$$RG = \frac{p-1}{p+1} \tag{4.22}$$

Compared with Hakki and Paoli's method, Cassidy's method can be used more accurately to determine the reflectivity of an AR-coated diode laser by measuring the RG product before and after coating. Practically, the integral over one mode is obtained by summing N equally spaced intensity measurements, and then taking an average. This approach is then called the mode sum/min method. Cassidy's method therefore has a larger data storage requirement.

Cho and co-workers [64] have shown that Cassidy's method is superior to other methods for gain evaluation of diode lasers, and confirmed the comparatively lower sensitivity of this technique to the instrument response function compared to the Hakki and Paoli one. Because of the improvement in signal to noise ratio (SNR) in Cassidy's method, it does not require a correction if errors of less than 5% can be tolerated [64].

The devices used in the experiments were InGaAsP/InP MQW lasers at different wavelength regions. The cavity lengths of the diode lasers ranged from 300μm to 1500μm. Uncoated diode lasers were driven at 85-95% of the original threshold current to investigate the bias current effect on reflectivity estimate. The temperature was set to 20^0C and kept constant by a Peltier cooler. For using a HP70951B Optical Spectrum Analyzer (OSA), the diode laser output was coupled into an optical fiber with an angled facet end (~ 45^0), which greatly reduced the feedback from the fiber end during the measurements (in this measurement system, the fiber end could be brought to the laser bar as close as 200 ~500 micron under microscope, and no collimating lens was used between the diode laser and the fiber). For using an Anritsu MS9710C Optical Spectrum Analyzer, F220FC-C / F230FC-C Connectorized Collimation Packages (AR-coated for 1050 ~ 1550nm) were used. The ASE spectra were measured with wavelength resolutions of 0.05, 0.1, and 0.2 nm to investigate the effect of finite wavelength resolution on the reflectivity evaluation. The resolution ranged from 0.05 to 0.2nm for the Anritsu MS9710C OSA, and from 0.05 to 0.1nm for HP70951B OSA, and were found reasonable in avoiding the deterioration of the data quality. The data presented in this work were all measured with 0.05nm resolution / 5nm span for the Anritsu OSA, and 0.1nm resolution / 5nm span for the HP OSA.

After depositing the AR coating on one facet, the diode laser was driven at the same bias current level and the ASE spectra were measured again with the same wavelength resolution. An example of the measured ASE spectra of a diode laser before and after the coating, biased at 90% of the original threshold current is shown in Figure 4.6. The AR coating simulation, both measured and then calculated reflectivity data points are shown in Figure 4.7. The diode laser and AR coating parameters were taken from Table 3.1(a).

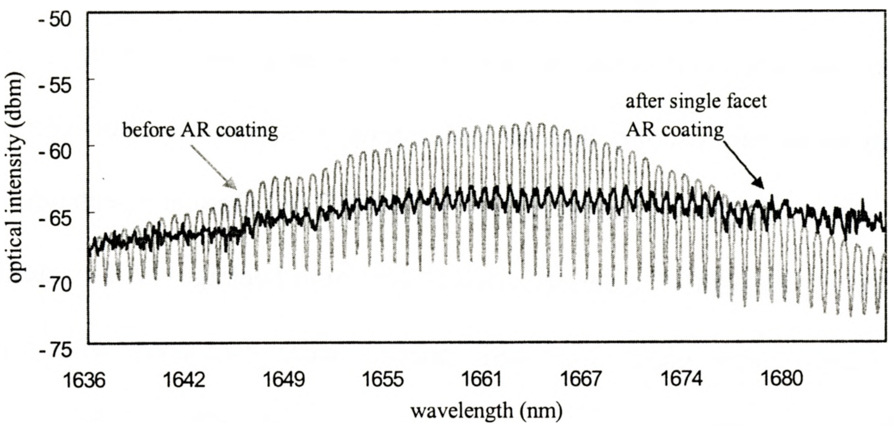

Figure 4.6 Measured ASE spectra of a 1.66 μm single QW diode laser before and after AR coating with wavelength resolution of 0.1nm, biased at the same current level.

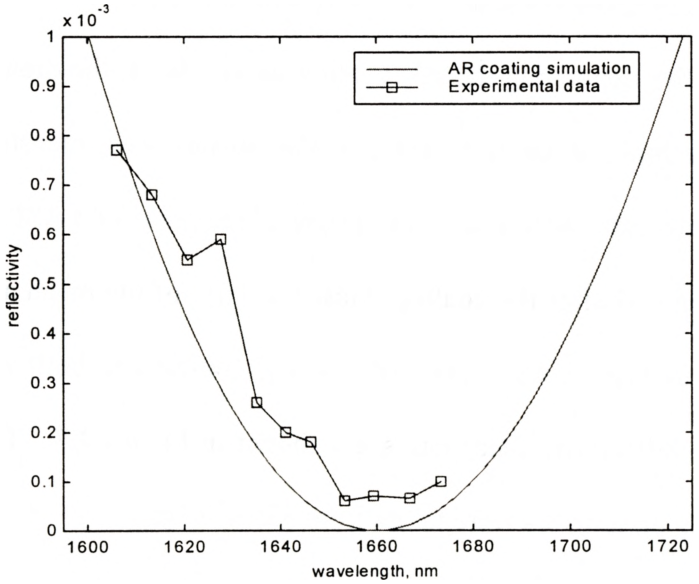

Figure 4.7 Simulated reflectivity curve and measured experimental data points

4.6 SUMMARY

In this chapter the fabrication of AR coatings on diode laser facets has been discussed. Real time monitoring of the optical thin films is the key to obtaining low reflectivities. The deposition process, e.g., the pressure in the chamber during coating, the gas mixture ratios, and the deposition rate should be optimized for this case to ensure high quality thin films.

CHAPTER 5

GRATING-EXTERNAL-CAVITY DIODE LASERS

5.1 INTRODUCTION

Diode lasers are known to be highly susceptible to optical feedback induced by reflections from outside the laser cavity. Under proper circumstances this undesirable effect can, however, also be used as an advantage. The static, dynamic, and spectral properties of the laser may be considerably influenced by coupling a portion of the diode laser output back into the laser cavity in a controlled fashion. Such intentional optical feedback from an external reflective element allows for an effective control of, e.g., the threshold gain, the emission wavelength, as well as the linewidth and mode stability of the diode laser.

In general, the behavior of a diode laser in an external cavity can be highly complicated, with the details depending on the feedback level, the external cavity length, the diode laser parameters, and on the optical power level. In an attempt to classify the behavior, five distinct operating regimes are identified [4], depending on the fraction of light that is fed back into the laser cavity; and reference [65] presented an updated and more detailed discussion. The five regimes are:

I. With very low levels of feedback, line narrowing or broadening is observed depending on the phase of the returned light. The external-cavity diode laser will show stable operation.

II. In the second regime, mode hopping is observed for light returned out of phase with the laser field. The lasing mode jumps between two external cavity modes, closely spaced in wavelength. In this case, the time-averaged spectrum of the diode laser will have two peaks, each corresponding to one of the possible modes.

III. In regime III, which is a very narrow region with feedback levels of –45 dB to –39 dB, the diode laser operates in a stable single mode with a narrow linewidth. The mode hopping in this regime is suppressed, and the laser remains sensitive to other reflections of comparable or greater magnitude.

IV. With higher feedback levels, line broadening by several orders of magnitude is observed; this phenomenon is known as "coherence collapse" [66] because of the drastic reduction in the coherence length of the laser. A diode laser operating in this regime is unsuitable as a narrow linewidth source. In this regime there is also a strong increase in the intensity noise of the diode laser.

V. In regime V, where the feedback levels are higher than –10 dB, stable single mode oscillation with a very narrow linewidth occurs again. This level of feedback is obtained only when the facet through which light is fed back into the laser cavity is AR coated. In this regime, the laser ideally operates in a long cavity with a short active region and the feedback dominates the field in the diode laser. The linewidth in this configuration is narrowed for all phases of returned light, and is generally insensitive to all other reflections.

It is important to note that only in regimes III and V is the laser line always narrowed by the feedback. Regime III, however, requires controlling the reflected power to be between –45 dB to –39 dB. This in turn, results in extreme sensitivity to additional weak reflections. Only in regime V is the laser narrowed for all feedback phases, and insensitive to additional reflections. This regime can be attained for AR-coated diode lasers.

During the past years, extensive work has been done on linewidth enhancement factors utilizing short external cavity (SXC) diode lasers [67]. It was found that the linewidth enhancement factors strongly depend on the emission wavelengths, and are fairly independent of the output powers for SXC diode lasers. Bonnell and Cassidy [68] have found that the fraction of light reflected back to the diode laser is less than 5×10^{-4} for a short external cavity. Some other workers have also estimated the amount of light feedback to the diode laser [69,70]. The accurate value depends on the dimension of the laser waveguide and often time is difficult to obtain.

Although it is relatively easy to construct a SXC diode laser, its tunable range is limited to 10 ~ 30 nm compared with 20 ~ 100 nm tunable range for a GEC diode laser [71]. In the SXC configuration, the side mode suppression ratio (SMSR) for short external cavity length L_e (50 μm, for example) is limited because the frequency selectivity of the external cavity is reduced, and modes adjacent to the lasing mode are also reinforced; as L_e increases further, the single longitudinal mode (SM) tuning decreases because the amount of optical feedback is reduced and, more importantly, because other modes resonant with the external cavity are enhanced. As a result, the tunable range for SXC diode lasers is limited by adjacent side modes for short L_e and resonant external cavity modes for long L_e. Therefore, in this work a GEC diode laser was used in spite of its complex construction and operation.

To ensure stable operation of external-cavity diode lasers in regime V, it is necessary to provide an AR coating to the laser facet facing the external cavity. Such a coating prevents the laser from operating in a mode determined purely by the laser facets and forces it to operate in a mode determined by the external reflector.

A grating-tuned external-cavity diode laser is outlined in Figure 5.1. The diode laser acts as a gain medium in the coupled cavity. In this work, it was mounted on a Peltier cooler. The reflection grating, facing the AR-coated facet, was held in a gimbal mount, and placed about 10 ~ 15 cm away from the diode laser. The grating was placed with grating lines perpendicular to the diode laser junction plane (this placement will be further discussed in section 5.4.1). Between the grating and the AR-coated facet, a collimating lens was used to couple the highly divergent emission from the diode laser to the grating. A He-Ne laser was used during the optical alignments so that the grating was in a plane that is parallel to the laser facet. Light transmitted through the uncoated facet of the diode laser was collimated and focused to a single mode fiber through F220FC-C/ F230FC-C Connectorized Collimation Packages (AR-coated for 1050 ~ 1550nm, not shown in Figure 5.1), and the spectrum was recorded by an Anritsu MS9710C Optical Spectrum Analyzer.

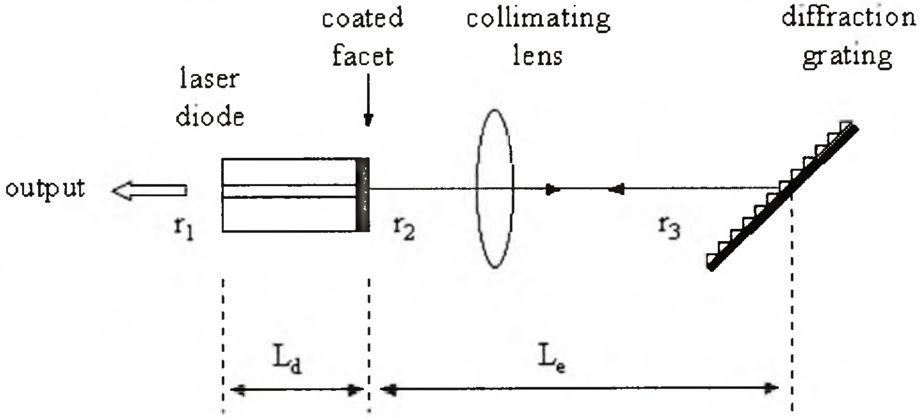

Figure 5.1 The grating-external-cavity (GEC) diode laser scheme

In the following sections, the grating-tuned external-cavity diode laser, operating in Regime V is discussed. The theoretical background of the diffraction grating and the tuning properties of the grating-external-cavity (GEC) diode laser are given. The grating response is calculated to determine the selectivity provided by the grating. The single longitudinal-mode oscillation of the external cavity is discussed. In the final part of the chapter, the experimental results for the single mode oscillation and the tuning range measurements are presented.

5.2 DIFFRACTION GRATINGS

Diffraction gratings have been known for over 150 years. They are important dispersing elements in spectroscopic instruments. The function of a diffraction grating is to interact with a wave in such a way that it generates a series of further waves, traveling in different directions which are dependent upon the wavelength.

When a traveling wave encounters an obstruction with dimensions similar to its wavelength, some of the energy in the wave is scattered. If the obstruction is periodic, or indeed if there is a periodic variation of any parameter which affects the propagation of the wave, energy is scattered into various discrete directions or “diffracted orders”, and a structure which acts in this way may be referred to as a “diffraction grating”. From the point of view of a wave in a diffracted order, the effect of the grating is to change the direction of propagation, and the amount by which it does so depends upon the relationship between the wavelength and the period. In this way a grating can disperse a variety of wavelengths to form a spectrum. In practice most gratings consist of a suitable rigid substrate with an optical surface upon which are produced a series of equispaced parallel grooves.

The concept of blazing a grating is that each groove should be so formed that independently, it redirects the incident light in the direction of a chosen diffracted order. Thus, in a reflection grating each groove consists of a small mirror inclined at an appropriate angle.

In Figure 5.2, the light is incident at an angle θ_i and reflected at an arbitrary angle θ, where both are measured from the grating normal. The facet normal to the groove face makes an angle θ_b relative to grating normal. This angle is the blaze angle of the grating. One can adopt the sign convention that angles have the same sign when they are on the same side as the grating normal and opposite sign if the rays cross over the normal. The grating equation can be written [57b]:

$$d(\sin\theta_i + \sin\theta_m) = m\lambda \tag{5.1}$$

The blaze condition is satisfied when the angle of incidence with respect to the facet normal is equal to the angle of reflection from the facet, i.e.,

$$\theta_i - \theta_b = \theta + \theta_b$$

or $$\theta_b = (\theta_i - \theta)/2$$

or $$\theta = \theta_i - 2\theta_b$$

which shows us immediately that the facet angle depends upon the mounting in which the grating is used. A particularly simply case is that of the "Littrow mounting" in which the diffracted beam returns along the path of the incident beam. In this case, $\theta_i = -\theta$, and $\theta_b = \theta$, and the grating equation may be written

$$2d\,sin\theta_b = m\,\lambda \tag{5.2}$$

The majority of spectrometric systems use gratings in their first order and not far from the Littrow condition.

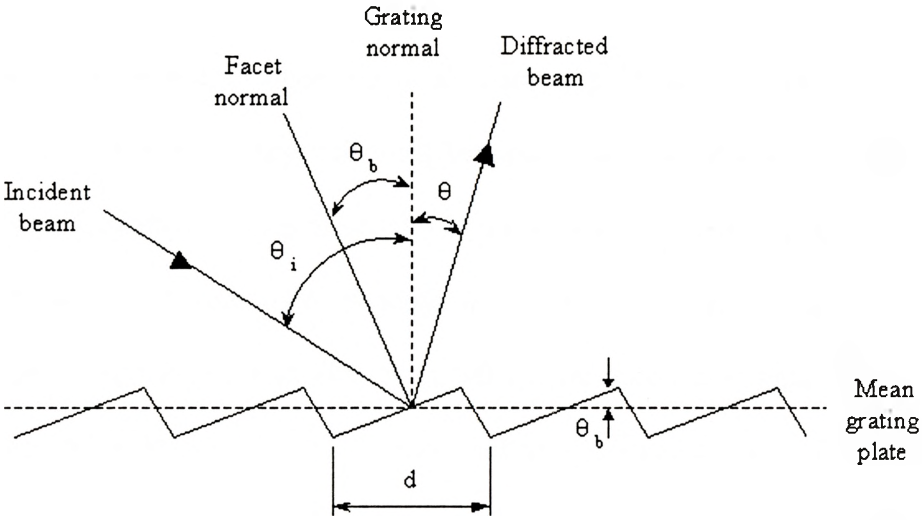

Figure 5.2 Determination of the facet angle for a blazed grating

5.3 MOUNTING THE GRATING

The grating used in this experiment is held in a gimbal mount with two angle-tuning screws that can be adjusted during the optical alignments and wavelength tuning. One angle scans across the grooves thereby selecting a different angle of diffraction for the first-order diffracted beam and, hence, a different oscillating wavelength. The other angle scans along the grooves and serves mostly for aligning of the diffracted beam back into the diode laser cavity.

The grating efficiency (energy distribution) depends on many parameters, including the power and polarization of the incident light, the angles of incidence and diffraction, the complex index of refraction of the metal (or glass or dielectric) of the grating, and the groove spacing. A complete treatment of grating efficiency requires the vector formalism of electromagnetic theory (i.e., Maxwell's equations), which has been studied in detail over the past few decades. Recently, computer codes have become commercially available that can accurately predict the grating efficiency for a wide variety of groove profiles over wide spectral ranges [72].

For blaze angles above $\sim 10^0$, the diffraction efficiency strongly depends on the orientation of the optical polarization with respect to the direction of the grooves [73]. A particularly useful regime for tuning external-cavity diode lasers is the range of blaze angles from about 18^0 to 38^0. For this regime, there is a broad plateau of high efficiency for $\theta_i > \theta_b$ when the incident polarization is perpendicular to the direction of the grating .

Typically the output radiation beam of the diode laser is characterized by two angles, which measure the divergence of the beam in the direction parallel and perpendicular to the junction plane. Usually, the beam divergence in the perpendicular direction is much broader than in the parallel direction and hence more lines on the grating will be illuminated if the grating is mounted with the grooves parallel to the junction plane. However, the highest first-order grating reflection can be obtained only when the electric field vector is perpendicular to the grooves [74].

The efficiency behavior of blazed gratings may be divided into six blaze angle regions [75]:

I. Very-low blaze angle gratings ($\theta_b < 5^0$) exhibit efficiency behavior that is almost perfectly scalar; that is, polarization effects are negligible.

II. For low blaze angle gratings ($5^0 < \theta_b < 10^0$), polarization effects begin to arise. The *S*-plane (*S*-plane has the electric vector perpendicular to the grooves) efficiency peak, always 100%, occurs exactly at the blaze angle or wavelength. The *P*-plane (electric vector parallel to the grooves) efficiency peak, always less (90% typical), is shifted slightly to shorter wavelengths. It is characteristic for all *P*-plane efficiency curves to decrease monotonically from their peak to zero, as λ / d increases to its limiting value of 2. Even though the wavelength band, over which 50% efficiency is attained in un-polarized light, is from $0.67\lambda_b$ to $1.8\lambda_b$, gratings of this type (with 1200 grooves per millimeter, for example) are widely used, because they most effectively cover the wavelength range between 200 and 800 nm (in which most ultraviolet-visible spectrophotometers operate).

III. Medium blaze angle gratings ($10^0 < \theta_b < 18^0$) show stronger polarization effects. For un-polarized light the efficiency is simply the arithmetic average of the *S*-plane and *P*-plane efficiencies.

IV. Low-anomaly blaze angle gratings ($18^0 < \theta_b < 22^0$) occupy a unique position. Special low *S*-plane anomaly is quite well maintained over a large range of angular deviations (the angle between the incident and diffracted beams), namely 25^0, but it depends on the grooves having an apex angle near 90^0. It may be noted that this minimal *S*-plane anomaly behavior is accompanied by the lowest first order *P*-plane peaks of any blazed grating, about 80%.

V. High blaze angle gratings ($22^0 < \theta_b < 38^0$) are widely used, despite the presence of a very strong anomaly in *S*-plane efficiency curves. For un-polarized light, the effect of this anomaly is greatly attenuated by its coincidence with the *P*-plane peak. A 50% efficiency is theoretically attainable in the Littorw configuration from $0.6\lambda_b$ to $2\lambda_b$, but in practice the long-wavelength end corresponds to such an extreme angle of diffraction that instrumental difficulties arise.

VI. Very-high blaze angle gratings ($38^0 < \theta_b < 64^0$) are rarely used in the first order; their efficiency curves are interesting only because of the high *P*-plane values.

The grating used in this work is a 600 line mm^{-1} ruled grating (blaze angle of 22.02^0 at 1.25 μm). This blaze angle falls in one of the six blaze angle regions, 22^0~38^0, which shows high grating efficiency and probably low anomaly for S-plane. Also in this region, there is a wide angular band in the S-plane over which very high efficiencies can be observed. This high S-plane efficiency shows a relatively flat curve over the λ/d range of 0.8~1.7. Meanwhile the effect of high P-plane efficiency is to reduce in practice the effect of the S-plane anomaly. Therefore this property is often used to maximum advantage when gratings serve as laser end mirror tuning elements.

Even after AR coating, the diode laser in the external cavity continues to emit radiation in the TE polarization (that is, the electric field vector lies in the plane of the junction); the TM polarized modes still have higher losses in the diode laser cavity. Therefore, in order to minimize losses in the overall cavity, the grating is mounted such that the grooves are perpendicular to the junction plane and hence the electric field vector. This arrangement is displayed in Figure 5.3.

The grating in this experiment was mounted in the Littrow configuration, i.e., the first order diffracted beam was reflected collinear with the incident beam and re-imaged onto the laser facet. Considerable care was taken to ensure that the grating was mounted vertically on the holder so that the two angle tilts were decoupled.

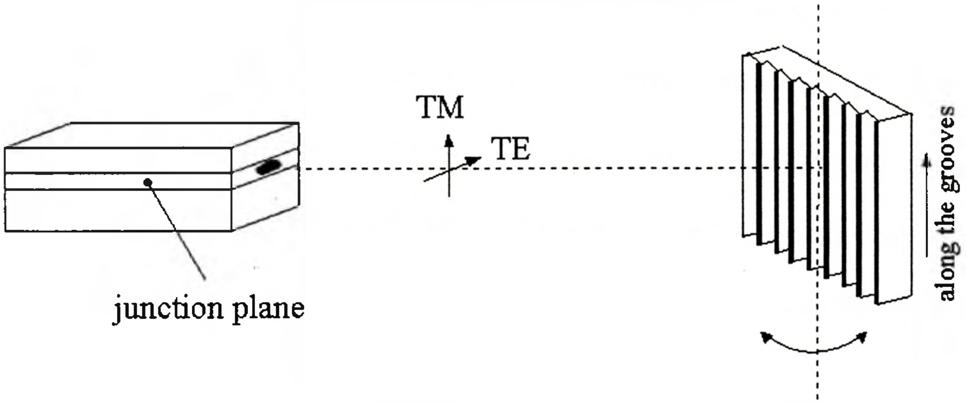

Figure 5.3 Figure showing how the grating is mounted with respect to the diode laser. The grooves are perpendicular to the electric field, which is parallel to the junction plane.

5.4 TUNING PROPERTIES OF EXTERNAL-CAVITY DIODE LASERS WITH DIFFRACTION GRATINGS

The solitary diode laser without external feedback has a multi-longitudinal mode spectrum with mode-spacing of approximately 0.2 ~ 0.8 nm (depending on the details of laser parameters). The purpose of optical feedback from the external cavity can be three fold:

1) to obtain single longitudinal mode oscillation,
2) to realize a broad-band tuning range,
3) to obtain a narrow spectral linewidth (i.e., highly coherent source).

To achieve these objectives the diode laser was coupled strongly to an external cavity loaded with a diffraction grating, shown in Figure 5.1. In this configuration the external cavity was the dominant cavity since the mode selection of the Fabry-Perot cavity (solitary diode laser) was partly destroyed by AR coating one of its facets.

5.4.1 The Diffraction Grating Response

The diffraction grating in a grating-tuned external-cavity diode laser can be viewed as a "reflection filter" with a certain reflection bandwidth $\Delta\nu$ (in some publications, $\Delta\nu$ is called reflection passband). The center frequency of this band is variably controlled by the angle of the grating. In this band, there could be a number of possible solutions to the external cavity resonance condition. This number N is dependent on the length of the external cavity L and is given by [76]:

$$N = (2L/c)\cdot\Delta\nu \tag{5.3}$$

The reflection bandwidth $\Delta\nu$ of the grating can be accurately determined by solving the boundary value problem for diffraction of the electromagnetic waves by a periodic boundary, taking into consideration the direction, polarization and amplitudes for the various waves. This is covered extensively in reference [73]. For the purpose of this thesis, it is sufficient to determine $\Delta\nu$ from a scalar aspect of diffraction having to do with the image-forming characteristics of the diffracted waves, when they are limited in size by gratings of the finite width. Therefore the formula used for the calculation of $\Delta\nu$ of the grating filter is:

$$\Delta\lambda = \lambda / (m N_{eff}) \tag{5.4}$$

where m is the order of scattering, and

$$N_{eff} = 2a / (d \cos\varphi) \tag{5.5}$$

is the effective number of illuminated lines of the grating, and

$2a =$ spot size of the incident beam

$d =$ grating constant (line spacing)

$\varphi =$ incident angle

In this experiment, the first-order diffracted beam was fed back into the laser cavity by a 600 line mm^{-1} ruled grating (Edmund Scientific E43746). The incident angle, φ, can be determined from the grating equation, Eq(5.2), because the incident angle and the first-order beam are collinear.

The spot size of the beam incident on the grating is determined using the following formula and assuming a Gaussian beam [57c]

$$w(z)^2 = w_0^2 \left[1 + \left(\frac{\lambda z}{\pi w_0^2 n} \right)^2 \right] \tag{5.6}$$

where

$w_0 =$ minimum spot size at $z = 0$ (spot size of the source)

$z =$ distance between source and lens

$n =$ refractive index of the medium of propagation

and $w(z)$ is the distance at which the field amplitude is down by a factor *1/e* compared to its value on the axis. Figure 5.4 shows these parameters graphically.

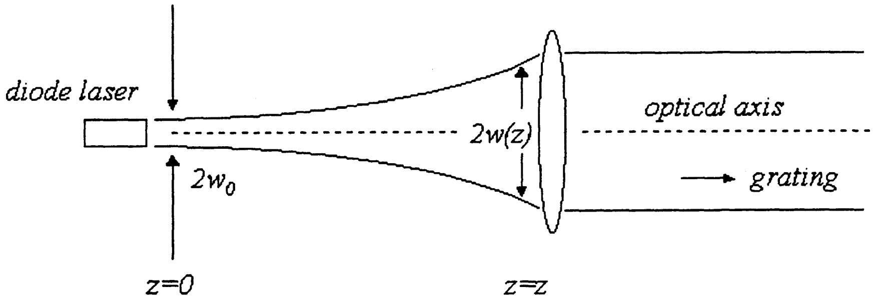

Figure 5.4 Geometry for determining the spot size of the beam incident on a diffraction grating

The spot size w_0 at the laser can be determined from a transcendental equation [77]:

$$\exp[(\pi w_0/\lambda)^2 \sin^2(\theta_{//}/2)] = 1.414\cos^2(\theta_{//}/2) \qquad (5.7)$$

where $\theta_{//}$ is the laser far field pattern divergence angle at $1/e$ of the field amplitude in the direction parallel to the junction. Typically, for ridge-waveguide diode lasers, $\theta_{//} = 10^0 \sim 25^0$ [74]. The following values are used to roughly determine $w(z)$:

$\lambda = 1.55\ \mu m$

$\theta_{//} = 15^0$

$w_0 = 2.206\ \mu m$ (calculated value using Eq(5.7))

z = 1.8 cm (measured distance between diode laser and collimating lens)

hence,

$$w(z) \cong 4.03 \text{ mm}$$

Now therefore, the FWHM of the grating response is determined by substituting the value for $w(z)$ (which in this case equals to a) into Eq(5.5), and then Eq(5.5) into Eq(5.4):

$$\Delta\lambda = \frac{\lambda\, d \cos\varphi}{2a} = 0.28 \text{ nm}$$

therefore

$$\Delta\nu = \frac{c}{\lambda^2}\Delta\lambda = 35 \text{ GHz}$$

The grating response indicates that a band of frequencies (and not a single frequency) is reflected by the grating back onto the laser facet.

Typically, the diode laser internal modes are about ~ 100 GHz apart. Therefore one can conveniently conclude that, although the light is reflected in a band of frequencies, this band will not include the next internal mode of the diode laser, that is, only one diode laser internal mode will be selected at a given orientation of the grating. However, the band of frequencies reflected from the grating may involve several external-cavity modes (depending on the length of the external cavity). Therefore, some external-cavity modes may acquire enough gain (from spontaneous emission noise, for example) for oscillation. However, the tendency of the diode laser would be to oscillate on a mode located at the peak of the grating response, since that mode would have the lowest optical loss and/or highest gain [78]. As a result, the gain discrimination can be strong enough so as to force the laser to oscillate at the wavelength for which the external feedback is strongest even though the free-running laser wavelength may have drifted many nanometers away from it. Therefore, the external-cavity mode closest to the grating passband central wavelength will be selected.

5.4.2 Theory of Grating-Tuned External-Cavity Diode Laser

Consider a grating-external-cavity (GEC) diode laser configuration of the type depicted in Figure 5.1. Here a diode laser, represented by an active medium in a short optical cavity with plane mirrors, is coupled to a much longer external cavity having a frequency selective and tunable reflective grating. The amplitude reflectivities of the diode facets are r_1 and r_2 and that of the external reflector at the oscillation frequency ω, including all external losses, is $r_3(\omega)$.

In the case of strong external optical feedback with the AR-coated facet facing the grating, the amplitude reflectivities of the AR-coated diode laser facet and the external reflector are related as $r_2 << r_3$. The lengths of the internal diode laser cavity and the external cavity are L_d and L_e, respectively, and the refractive index of the active medium is n_d . The round-trip times inside the internal and the external cavity are:

$$\begin{cases} \tau_d = 2n_d L_d / c \\ \tau_e = 2L_e / c \end{cases} \tag{5.8}$$

respectively, with c being the velocity of light in vacuum.

This coupled-cavity configuration can be conveniently analyzed as a simple two-mirror laser structure by replacing the diode laser output facet reflectivity r_2 by a complex-valued effective amplitude reflection coefficient $r_{eff}(\omega)$, which takes into account the effects of both r_2 and $r_3(\omega)$. Considering the multiple reflections of the laser diode facet, by keeping the r_2 surface as a reference plane, $r_{eff}(\omega)$ takes the form [79,80]:

$$r_{eff}(\omega) = r_2 - \left(1 - r_2^2\right) r_3(\omega) \sum_{p=1}^{\infty} \left[r_2 r_3(\omega)\right]^{p-1} e^{jp\omega\tau_e} \tag{5.9a}$$

or

$$r_{eff}(\omega) = \frac{r_2 + r_3(\omega) e^{j\omega\tau_e}}{1 + r_2 r_3(\omega) e^{j\omega\tau_e}} = \left|r_{eff}(\omega)\right| e^{j\varphi} \tag{5.9b}$$

The expression in Eq(5.9) appears as the geometric sum of multiple reflections. This approximation ignores the contributions from higher order transverse modes being scattered at the laser mirror and reflected back into the fundamental transverse mode of the laser.

The round-trip condition for steady-state operation of the coupled-cavity laser can be expressed as:

$$r_1 e^{(g_{th} - \alpha_m) L_d} \cdot e^{j\omega\tau_d} \cdot r_{eff}(\omega) = 1 \tag{5.10}$$

where g_{th} is the threshold gain and α_m represents the mode loss. Using Eq(5.10), the threshold gain is determined by:

$$g_{th} = \alpha_m - \frac{1}{L_d} \ln\left(r_1 \left| r_{eff}(\omega) \right|\right) \tag{5.11}$$

From Eq(5.11), it can be seen that the threshold gain of the diode laser in external cavity changes as the tuning wavelength changes. This will be shown explicitly in Figures 5.7, 5.11, and 5.15 in section 5.5.

The mode frequency ω satisfies the phase condition

$$\omega \cdot \tau_d + \varphi(\omega) = 2m\pi \tag{5.12}$$

where m is an integer, and from Eq(5.9b), after some mathematical work,

$$\varphi(\omega) = \tan^{-1}\left(\frac{r_3\left(1 - r_2^2\right)\sin(\omega \cdot \tau_e)}{r_2\left(1 + r_3^2\right) + r_3\left(1 + r_2^2\right)\cos(\omega \cdot \tau_e)} \right) \tag{5.13}$$

is the feedback-induced phase shift. Therefore, Eq(5.12) can be conveniently written as:

$$(\omega - \omega_m) \cdot \tau_d + \varphi(\omega) = 0 \tag{5.14}$$

where $\omega_m = 2m\pi / \tau_d$ being the frequency of m^{th} longitudinal mode of the solitary diode laser without optical feedback. For each individual mode ω_m, Eq(5.14) can be used to obtain the lasing frequency ω, while Eq(5.11) determines its threshold gain.

In the case of wavelength-dependent feedback, r_3 is a function of ω. Although the exact form of $r_3(\omega)$ depends on the specific feedback element used (grating, reflection filter, etc.), one can formally write

$$|r_3(\omega)|^2 = R_3 f(\omega - \omega_0/\gamma_0) \tag{5.15}$$

where R_3 is the peak reflectivity occurring at ω_0, and γ_0 is a measure of the spectral width over which significant feedback occurs. Therefore, the oscillation frequency ω can be conveniently expressed in the following form [78]:

$$\omega = \frac{(\omega_m + \beta \cdot \omega_0)}{(1+\beta)} \tag{5.16}$$

where β is a dimensionless parameter given by

$$\beta = \left(\frac{\sqrt{R_3}(1-R_2)}{\sqrt{R_2}(1+R_3) + \sqrt{R_3}(1+R_2)} \right) \frac{\tau_e}{\tau_d} \tag{5.17}$$

and $R_2 = r_2^2$ is the reflectivity of the facet facing the external reflector.

Eq(5.14), Eq(5.16) and Eq(5.17) are of crucial importance when analyzing the tuning performance of external-cavity diode lasers with strong feedback. Eq(5.16) shows the pulling of the FP mode towards ω_0, the frequency at which the feedback is strongest. This mode-pulling phenomenon is similar to that occurring in solid-state and gas lasers where the FP mode is pulled toward the gain peak. The parameter β in Eq(5.17) is also known as "stabilization factor", and can be made large by decreasing R_2, by increasing R_3, and by making the external cavity longer than the laser cavity $(\tau_e > \tau_d)$. When β is made large enough, from Eq(5.16), one can see that $\omega \to \omega_0$. This is the basis of the mode-pulling effect in external-cavity diode lasers with a wavelength selective element.

In this work, decreasing R_2 is achieved through AR coating of the diode laser facet facing the grating. The value of R_3 depends not only on the grating reflectivity but also on the coupling and propagation losses encountered by the mode during a round trip inside the external cavity. Therefore, if one wants to increase R_3, the losses in the external cavity should be minimized.

During the tuning operation, for each orientation of the grating, the grating dispersion selects an external-cavity mode with the minimum threshold gain to oscillate within the internal cavity mode considered. The tuning of the grating dispersion profile relative to the frequency comb of external-cavity modes will determine the finer details of the tuning characteristics of the laser. Consequently, by rotating the grating, continuous wavelength tuning over several external-cavity mode spacing can be accomplished.

5.4.3 Tuning Range Measurements

A careful initial alignment of the grating, collimating lens, and optical detector is required. Small adjustments of the grating rotation screws should smoothly shift the laser wavelength. At the very end of the tuning range, since the gain cannot compensate for the cavity losses, the laser will not oscillate. In another case, if the AR coating was not perfect (such as the AR coating bandwidth being less than the gain bandwidth), the laser output would be seen to hop back and forth or share power between two very different frequencies (this phenomenon was often found when tuning a diode laser without AR coating).

One is the fixed "free-running" wavelength at which the laser will operate if there is too little or no feedback from the grating; the other is the angle-dependent wavelength set by the grating feedback.

Tilting the grating should tune the output wavelength over a certain range, depending on the particular laser parameters and structure, and the amount of feedback from the diffraction grating. With grating rotation the lasing wavelength moves with mode jumping from one longitudinal mode to the next one. The choice of which mode the laser will hop to next is often extremely sensitive to optical feedback. If the grating or the lens is misaligned, the output wavelength will either be insensitive to small changes of the grating angle or will move only a small amount and then jump backwards.

5.5 EXPERIMENTAL RESULTS AND DISCUSSION

Three different diode laser structures were used in this work. All of them are of ridge waveguide structures, and were put in grating-external-cavity (GEC) set-ups in the Littrow configuration. The output power before and after AR coating was measured, shown in Figures 5.5, 5.9 and 5.13, respectively, for three different laser structures. The threshold current was found to increase for the GEC diode laser with one facet AR-coated, compared to a solitary diode laser without AR coating. This is shown in Figures 5.6, 5.10 and 5.14, respectively. Threshold currents as a function of emission wavelength were also measured for each individual laser structure in GEC configuration, shown in Figures 5.7, 5.11 and 5.15, respectively. The points in those curves correspond to emission wavelengths selected by rotating the reflection grating. The tuning ranges for three different laser structures are displayed in Figures 5.8, 5.12 and 5.16, respectively. At the end of this section, the experimental results are summarized in Table 5.1.

5.5.1 1.66 μm Single Quantum Well Diode Laser

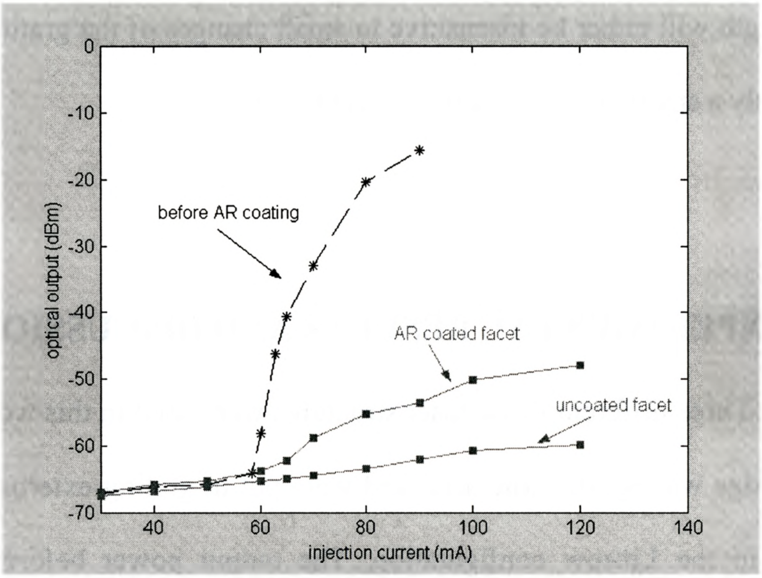

Figure 5.5 The injection current versus output power for a 1.66 μm diode laser. Dashed and solid lines correspond to before and after AR coating of the solitary diode laser, respectively. The diode laser temperature was 20^0C in all cases.

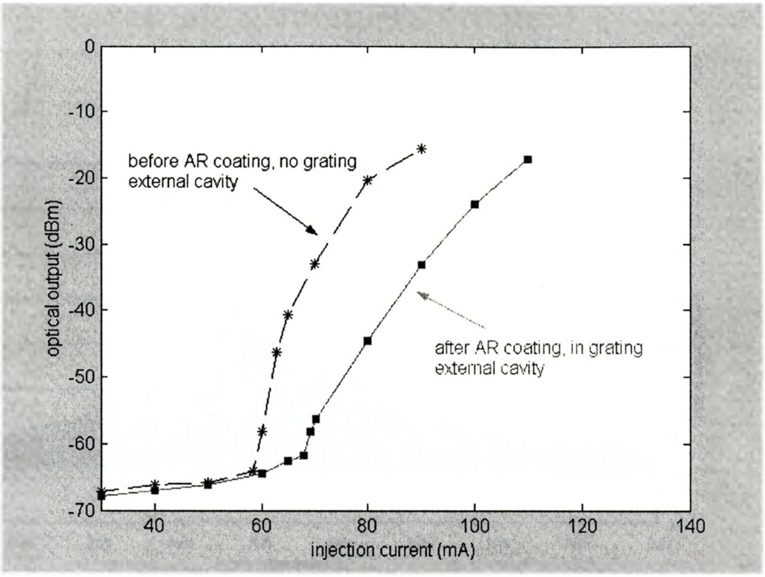

Figure 5.6 The injection current versus output power for a 1.66 μm diode laser. The dashed line represents a solitary diode laser without AR coating. The solid line represents an AR-coated diode laser in grating external cavity (GEC) configuration. The diode laser temperature was 20^{0}C in all cases.

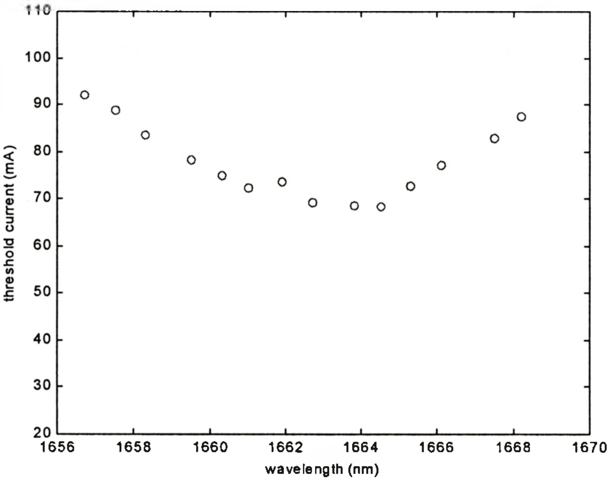

Figure 5.7 Threshold currents of a 1.66 μm AR-coated diode laser in grating-external-cavity as a function of lasing wavelength.

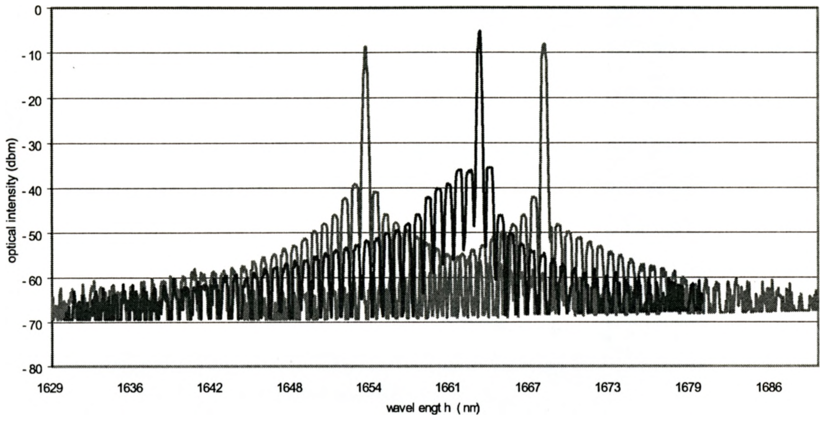

Figure 5.8 Grating-tuned output spectra for a 1.66 μm AR-coated diode laser. The left-most tuning wavelength is 1654.0nm, and the right-most is 1668.1nm.The tuning range is approximately 14.1nm.

The tuning range of GEC diode laser in this case was improved from 8.2nm without AR coating to 14.1nm with one facet AR-coated.

5.5.2 MQW Diode Laser (#3229)

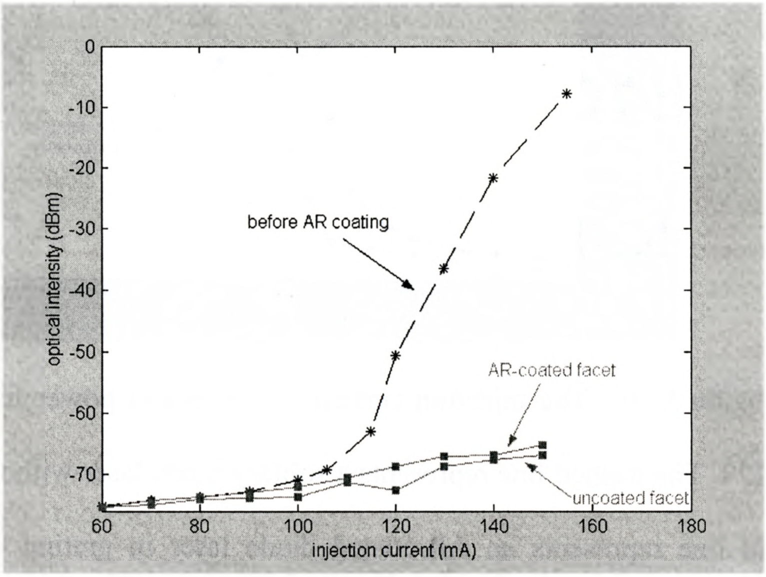

Figure 5.9 The injection current versus output power for MQW diode laser #3229. Dashed and solid lines correspond to before and after AR coating of the solitary diode laser, respectively. The diode laser temperature was 18^{0}C in all measurements.

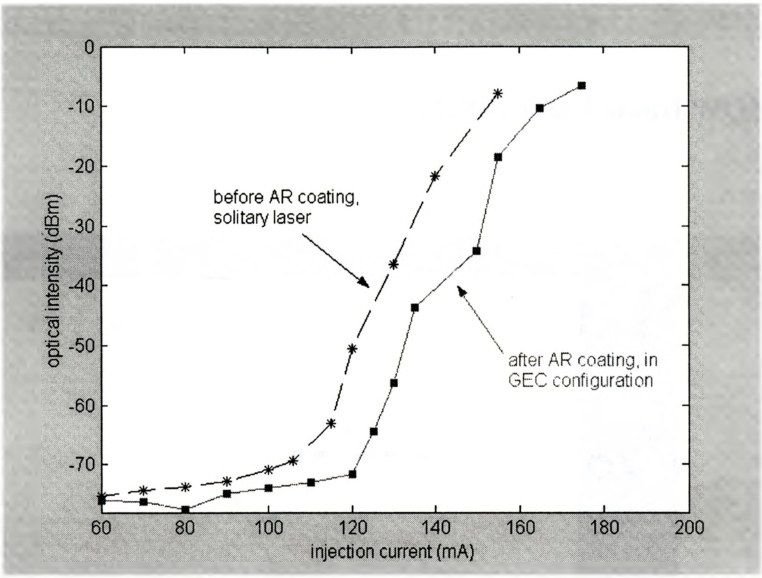

Figure 5.10 The injection current versus output power for MQW diode laser #3229. The dashed line represents a solitary diode laser without AR coating. The solid line represents an AR-coated diode laser in grating external cavity (GEC) configuration. The diode laser temperature was 18^0C in all measurements.

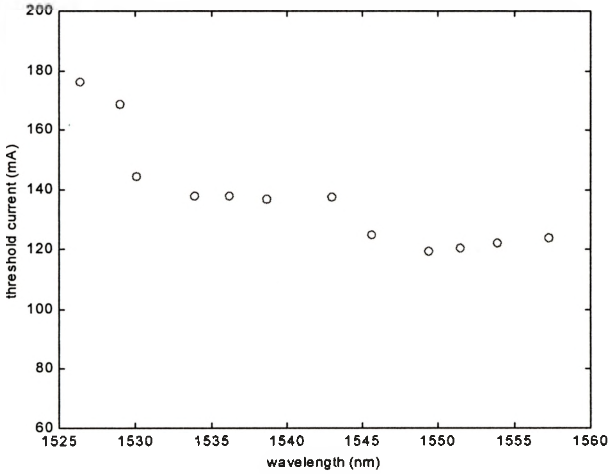

Figure 5.11 Threshold currents of AR-coated MQW diode laser #3229 in grating-external-cavity as a function of lasing wavelength.

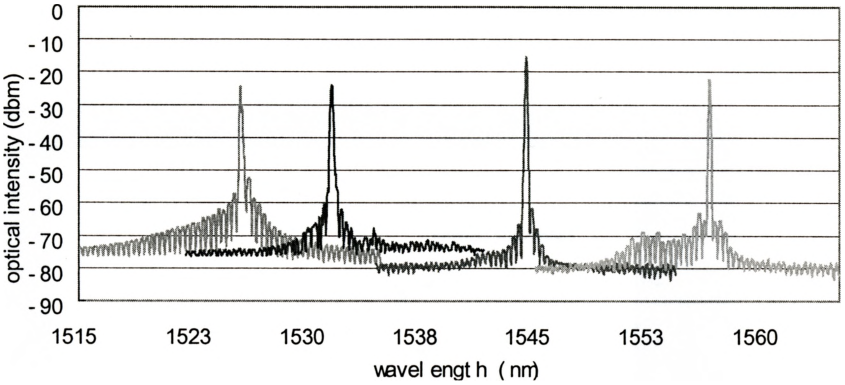

Figure 5.12 Grating-tuned output spectra for AR-coated MQW diode laser #3229. The left-most tuning wavelength is 1526.3nm, and the right-most is 1557.2nm. The tuning range is approximately 30.9nm.

The tuning range of the GEC diode laser in this case was improved from 26.1nm without AR coating to 30.9nm with one facet AR-coated.

5.5.3 MQW Diode Laser (#2452)

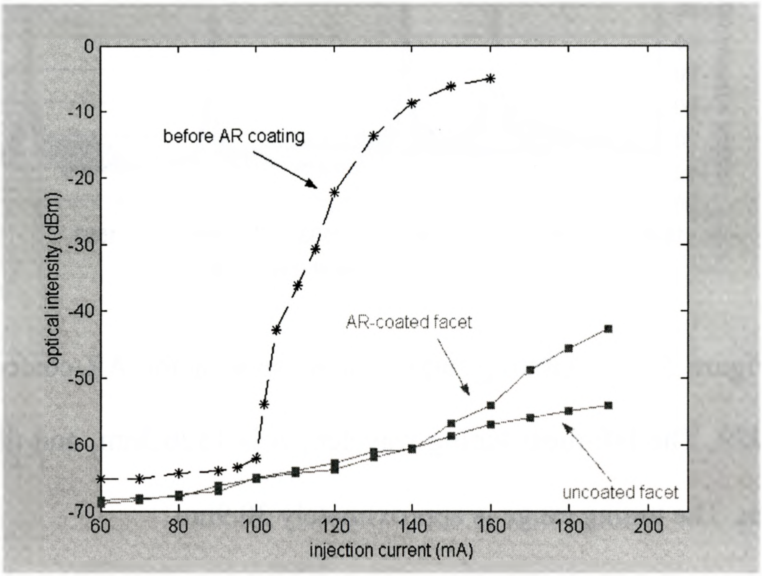

Figure 5.13 The injection current versus output power for MQW diode laser #2452. Dashed and solid lines correspond to before and after AR coating of the solitary diode laser, respectively. The diode laser temperature was 20^0C in all cases.

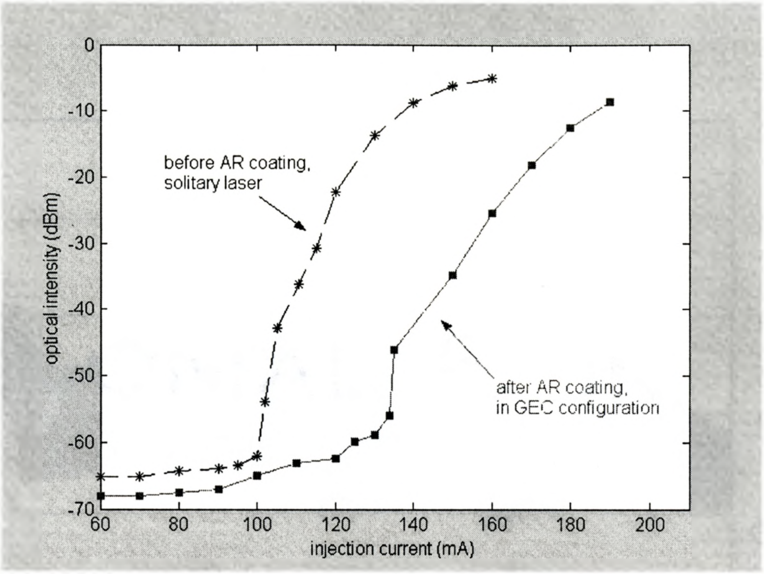

Figure 5.14 The injection current versus output power for MQW diode laser #2452. The dashed line represents a solitary diode laser without AR coating. The solid line represents an AR-coated diode laser in grating external cavity (GEC) configuration. The diode laser temperature was 20^0C in all cases.

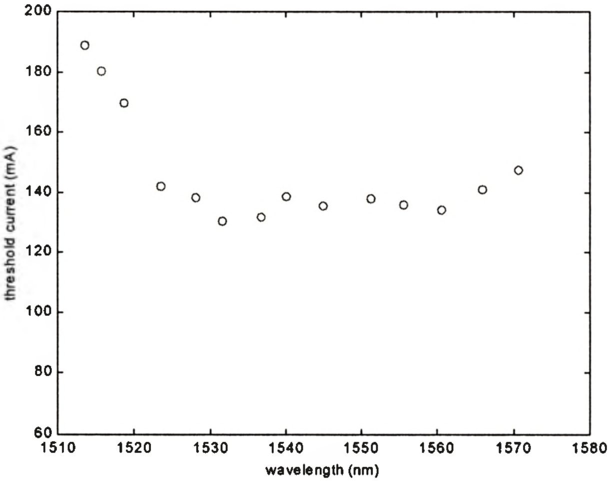

Figure 5.15 Threshold currents of AR-coated MQW diode laser #2452 in GEC configuration as a function of lasing wavelength.

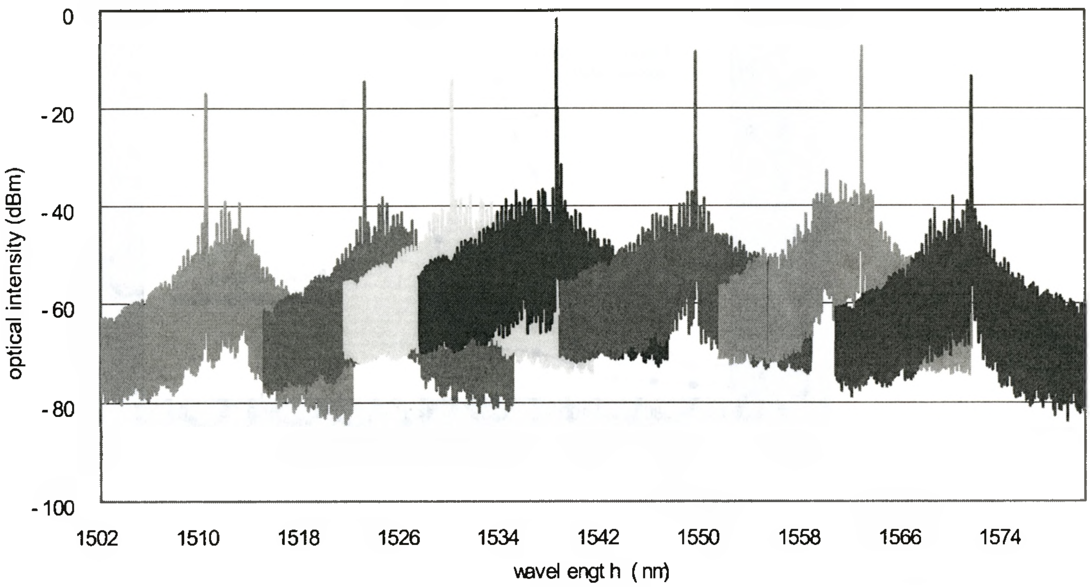

Figure 5.16 Grating-tuned output spectra for AR-coated MQW diode laser #2452. The left-most tuning wavelength is 1509.8nm, and the right-most is 1571.1nm. The tuning range is approximately 61.3nm.

The tuning range of the GEC diode laser in this case was improved from 49.0nm without AR coating to 61.3nm with one laser facet AR-coated.

5.5.4 Summary of Experiments and Discussion

The results of the experiments completed in this work are summarized in Table 5.1.

Table 5.1 Summary of tuning properties

diode laser	threshold current I_{th} (mA) *		tuning range (nm)	
	solitary DL	AR-coated GEC DL	no AR-coating GEC DL	AR-coated GEC DL
1.66 μ m SQW DL	58.5	67.8	8.2	14.1
MQW DL #3229	105.9	125.1	26.1	30.9
MQW DL #2452	102.0	133.8	49.0	61.3

* for AR-coated GEC diode lasers, the threshold current I_{th} was measured at the central wavelength

The diffraction grating is an important element for the GEC diode lasers, investigated in this work. First, it provides wavelength selection and thereby limits the number of "possible solutions" of the external-cavity modes (depending upon the FWHM of the grating response). Second, the use of a grating (frequency selective device) in the external cavity enables laser operations to occur at frequencies away from the frequency that satisfies the minimum threshold condition. The minimum threshold condition forces the laser to operate at a frequency where the external-cavity phase ($\omega \times \tau_e$, where τ_e is the round trip time in the external cavity and ω is the operation frequency) is equal to an integral multiple of 2π. With grating feedback, the operation frequency is determined by Eq(5.12), and the phase of the returned light is not critical because the internal mechanism of the laser cavity adjusts the overall gain to compensate for the phase mismatch.

Since the AR coating and the short cavity length were necessary to suppress the FP modes of the cavity to allow the feedback from the grating to determine the lasing wavelength, the optimum tuning range could be obtained when the wavelength of minimum reflectivity of the AR coating was aligned to the peak in the spontaneous emission. Therefore, the tuning ranges that can be obtained with an AR-coated external- cavity laser depend on the quality of the AR coating as well as on the fraction of energy that is coupled back into the diode laser [4,74].

For some commercial GEC diode lasers in the Littrow configuration, the total tuning range is claimed to be increased by a factor of 2~3 after applying AR coating to the diode lasers [81], but no further details are given. For the diode lasers used in this work, the overall improvement in terms of tuning range is around 35% after AR coating. At this point, it deserves more investigations on how AR coatings further improve the tunability, along with the optimization of the external cavity and the design of broad-gain diode lasers.

CHAPTER 6

SUMMARY AND CONCLUSIONS

A semiconductor diode laser itself is a key device for optoelectronics owing to its superior performance such as small size, low power consumption, high efficiency, longer device lifetime, flexibility for selecting wavelength, and adaptability for photonic integrated circuits. A wavelength-tunable diode laser is a specific device, characterized by its wavelength tunability, and expected to be a key device for advanced optical communication, as well as for a variety of optical measurements and laser spectroscopy.

One of the key requirements for stable and a broad tunability of a grating-external-cavity (GEC) diode laser, as presented in this study, is high quality AR coating of one laser facet, which enables the diode laser to operate in a strong feedback regime. Therefore, this thesis is concerned with addressing this issue.

The scheme for obtaining a broad tuning range investigated in this thesis falls under the broad category of optical feedback. Light leaving one of the facets of the laser is coupled back into the laser cavity through the same facet, after being reflected from a diffraction grating. In order to make the diode laser operate in the scheme of a strong frequency selective feedback configuration, the facet through which the light is fed back has to be AR-coated.

To obtain very low reflectivities of AR coatings on diode laser facets, the effective refractive index of diode lasers must be calculated precisely, since it serves as the substrate in the AR coating design. The concept of optical detuning is applied to the design of multi-layer AR coatings. The fabrication by ECR-PECVD is a crucial process to obtain high quality AR coatings. The process parameters, such as pressure, gas mixtures ratio and deposition rate have to be controlled precisely. Real time monitoring of the refractive index and film thickness by *in situ* ellipsometry provides an essential measurement for optical thin-film growth.

The AR-coated diode lasers were then placed in an external cavity loaded with a diffraction grating. In this configuration, the laser oscillated in a stable single longitudinal mode with a side mode suppression ratio of more than 30 dB. In this work, the overall improvement of the tuning range, before and after AR coatings, was found to be 35%, still below some commercially available GEC diode lasers [81]. Therefore, further investigations are needed for the AR-coated GEC diode lasers.

Another important limitation to the tuning range is set by the width of the gain curve and gain flatness of the diode lasers. It is interesting to note that a tuning range of 240 nm has been achieved by using a grating reflector in an external-cavity configuration [82].

The width of the gain curve may be increased by using a combination of first- and second-quantized-state lasing in a quantum-well laser [83], or by using a quantum-well structure with non-identical (dimensional or compositional asymmetric) wells. Due to time constraints, these were not investigated in this thesis, and the whole project was necessarily limited in scope. Some suggestions for future work are as follows:

1) Deposition of a high reflection (HR) coating on the output facet of a diode laser [84], which can reduce the cavity losses at the tuning end, thereby increasing the tuning range;
2) Two-material, four-layer AR coating design using SiO_2/Si_3N_4, or SiO_2/a:Si combinations, which can greatly ease the thin-film depositions and real time monitoring compared to using SiO_xN_y;
3) Improvement of the optical feedback and coupling efficiency, such as using an AR-coated collimating lens and gold-coated diffraction grating in GEC configuration; and,
4) Determination of the diode laser linewidth obtained with GEC configuration [85], and investigation of the behavior at other wavelengths, i.e., obtaining a graph of linewidth versus wavelength.

APPENDIX A

PROGRAMS FOR CALCULATING THE EFFECTIVE REFRACTIVE INDEX OF A 2-D OPTICAL WAVEGUIDE

A.1 EFFECTIVE REFRACTIVE INDEX OF TE0 MODE

```
% effective refractive index of fundamental TE mode
clear
clf
ns=   ;     % refractive index of the substrate
nf=   ;     % refractive index of the film
nc=   ;     % refractive index of the cladding layer
t=      ;   % film thickness(nm)
lambda=      ;      % wavelength(nm)

ae=(ns.^2-nc.^2)./(nf.^2-ns.^2);            % asymmetry measure
v0=2*pi*t*sqrt((nf.^2-ns.^2))./lambda;

b=0:0.00001:0.99999;
v=(atan(sqrt(b./(1-b)))+atan(sqrt((b+ae)./(1-b))))./sqrt(1-b);

% find v vs b
s=size(v);
```

```
k=s(1,2);


q=1;
for w=1:k
   if v0-v(1,q)<0.00001
            r=q;     % find the position r in matrix v, same as matrix b
   else
            q=q+1;
   end
end
be=b(1,r);
neff=sqrt(ns.^2+be.*(nf.^2-ns.^2))        % the effective refractive index
neff1=num2str(neff);


plot(v,b,'r');
xlim([0 12]);
xlabel('v');
ylabel('b');
axs=axis;
scalex=axs(2)-axs(1);
scaley=axs(4)-axs(3);
title('Fundamental TE mode (3-layer waveguide)')


text(0.65*scalex,0.5*scaley,'the refractive index(TE) is:');
text(0.75*scalex,0.45*scaley,neff1);
text(0.1*scalex,0.95*scaley,'nc=');
text(0.15*scalex,0.95*scaley,num2str(nc));
text(0.1*scalex,0.9*scaley,'nf=');
text(0.15*scalex,0.9*scaley,num2str(nf));
```

```
text(0.1*scalex,0.85*scaley,'ns=');
text(0.15*scalex,0.85*scaley,num2str(ns));
text(0.30*scalex,0.9*scaley,'t=');
text(0.35*scalex,0.9*scaley,num2str(t));
text(0.42*scalex,0.9*scaley,'(nm)');
```

A.2 EFFECTIVE REFRACTIVE INDEX OF TM0 MODE

```
% effective refractive index of fundamental TM mode
clear
clf
ns=  ;    % refractive index of the substrate
nf=  ;    % refractive index of the film
nc=  ;    % refractive index of the cladding layer
t=   ;    % film thickness(nm)
lambda=   ;    % wavelength(nm)

b=0:0.00001:0.99999;
am=(nf.^4./nc.^4)*(ns.^2-nc.^2)./(nf.^2-ns.^2);    % asymmetry measure
qs=(ns.^2/nf.^2)./((1-b)+b.*ns.^4./nf.^4);
d=(1-ns.^2/nf.^2)./(1-nc.^2/nf.^2);
v0=2*pi*t*sqrt((nf.^2-ns.^2))./lambda;

v=(atan(sqrt(b./(1-b)))+atan(sqrt((b+am.*(1-b.*d))./(1-b))))./...
(sqrt(1-b).*sqrt(qs).*(nf./ns));

%find v vs b
s=size(v);
```

```
k=s(1,2);


q=1;
for w=1:k
   if v0-v(1,q)<0.00001
       r=q;    %find the position r in matrix v, same as matrix b
   else
       q=q+1;
   end
end
bm=b(1,r);
qs=(ns.^2/nf.^2)./((1-bm)+bm.*ns.^4./nf.^4);
% the effective refractive index
neff=sqrt(ns.^2+bm.*(nf.^2-ns.^2)./(nf./(ns.*qs).^2))
neff1=num2str(neff);


plot(v,b,'b');
xlim([0 12]);
xlabel('v');
ylabel('b');
axs=axis;
scalex=axs(2)-axs(1);
scaley=axs(4)-axs(3);
title('Fundamental TM mode (3-layer waveguide)')
text(0.65*scalex,0.4*scaley,'the refractive index(TM) is:');
text(0.75*scalex,0.35*scaley,neff1);


text(0.1*scalex,0.95*scaley,'nc=');
text(0.15*scalex,0.95*scaley,num2str(nc));
```

```
text(0.1*scalex,0.9*scaley,'nf=');
text(0.15*scalex,0.9*scaley,num2str(nf));
text(0.1*scalex,0.85*scaley,'ns=');
text(0.15*scalex,0.85*scaley,num2str(ns));
text(0.30*scalex,0.9*scaley,'t=');
text(0.35*scalex,0.9*scaley,num2str(t));
text(0.42*scalex,0.9*scaley,'(nm)');
```

APPENDIX B

PROGRAM FOR CALCULATING THE EFFECTIVE REFRACTIVE INDEX OF A MULTI-LAYER SLAB WAVEGUIDE

```
% effective refractive index of a multi-layer slab waveguide
clear
clf

n=[     ];        % refractive index sequence, start from substrate,
                  %end up with ambient(=1.0)
t=[     ];        % thickness(nm) sequence, start from substrate(=0),
                  %end up with top layer
lambda=   ;       % wavelength(nm)

k0=2.*pi./lambda;
belta=3.2*k0:0.00001:3.65*k0;      %define the range of belta

for j=1:length(n);
  p(j,:)=sqrt(belta.^2-(n(1,j).*k0).^2);
end

for k=1:length(belta);
```

```
  m1(:,:,k)=inv([1 1;-p(2,k) p(2,k)])*[1 1;-p(1,k) p(1,k)];
end

for j=2:length(n)-1;
  for k=1:length(belta);
    m(:,:,k)=inv([1 1;-p(j+1,k) p(j+1,k)])*[exp(-p(j,k).*t(1,j))...
              exp(p(j,k).*t(1,j));-p(j,k).*exp(-p(j,k).*t(1,j))...
              p(j,k).*exp(p(j,k).*t(1,j))];
  end
  for h=1:length(belta);
    m1(:,:,h)=m(:,:,h)*m1(:,:,h);
  end
end

a=abs(m1(2,2,1));
for k=2:length(belta);
  if abs(m1(2,2,k))<a;
    a=abs(m1(2,2,k));
    g=k;
  end
end

neff=belta(1,g)./k0    % the effective refractive index
                       %for multi-layer slab waveguide
a4(1,:)=abs(m1(2,2,:));  % zero element
plot(belta,a4)         % help to visualize the solution
ylim([0,10])

% the averaged effective refractive index based on reference [12]
```

```
sigmat=0;
for j=2:length(t)
  sigmat=sigmat+t(1,j);
end
sigmant=0;
for j=2:length(t)
  sigmant=sigmant+n(1,j).^2*t(1,j);
end
nave=sqrt(sigmant./sigmat)
```

APPENDIX C

PROGRAM FOR TRIPLE-LAYER AR COATING CALCULATION

(The calculation is composed of 3 programs: bcfunction, equivalentlayer, and 3layer. The detuning factor is given in the program-3layer, and practically the detuning factor is around 0.01~0.1. If the detuning factor is too small (less than 0.01, for example), the computing time is extremely long; if the detuning factor is too large, the result is not good enough. Depending on the computing speed of my computer, I found 0.03 is suitable.)

```
%%% [b,c] function
clear
clf

function y=bcfunction(n,d,lambda,nm);
for k=1:length(n);
  delta(k,:)=2.*pi.*n(1,k).*d(1,k)./lambda;
end

for f=1:length(lambda);
  m1(:,:,f)=[1 0;0 1];
end
```

```
for p=1:length(n);
  for j=1:length(lambda);
    m(:,:,j)=[cos(delta(p,j)) i.*sin(delta(p,j))./n(1,p);i.*...
       sin(delta(p,j)).*n(1,p) cos(delta(p,j))];
  end
  for q=1:length(lambda);
    m1(:,:,q)=m1(:,:,q)*m(:,:,q);
  end
end

for f=1:length(lambda);
  y(:,:,f)=m1(:,:,f)*[1;nm];
end




%%% equivalent Layers
% consider combinations of the form ABA
clear
clf

disp('This samll program will help you calculate the optical thickness ')
disp('of equivalent layers of the form ABA !')
disp('*****************************************************')

ne=input('Please enter the refractive index of the equivalent layer:  ');
na=input('Please enter the refractive index of material A:  ');
nb=input('Please enter the refractive index of material B:  ');
```

```
deltaA=0.5*acos((nb^2+na^2)*(ne^2-na^2)/((nb^2-na^2)*(ne^2+na^2)));
deltaB=atan(2*na*nb/(na^2+nb^2)/tan(2*deltaA));

disp(['the optical thickness of A is:  'num2str(deltaA/2/pi)])
disp(['the optical thickness of B is:  'num2str(deltaB/2/pi)])


%%% triple-layer AR-coating calculation
clear
clf

lambda0=   ;        % design wavelength(nm)
n0=1.0;             % refractive index of the ambient
nm=    ;            % refractive index of the substrate(the
                    %effective refractive index of the ridge
                    %waveguide laser structure)
rr=0.0001;          % design reflectivity
n=[      ];         % refractive index sequence, start with the film
                    % next to the ambient(=1.0)
detuningfactor=0.03;

% central design wavelength(one point) refining
lambda=lambda0;    %scanning range
k=1;  %initial of matrix(w)
for w1=0.1945:0.0001:0.1955;
  for w2=0.2385:0.0001:0.2395;
    for w3=0.7415:0.0001:0.7425;
           w=[w1 w2 w3];        %confinement factor
               d=w.*lambda0./4./n;       %film thickness, (quarter
```

```
                                        %wavelength)*(refinement factors)
              bc=bcfunction(n,d,lambda,nm);      %calculate [b;c],
                                                 %of which y=c/b
           y=bc(2,1,:)./bc(1,1,:);
          if real(y-n0)<detuningfactor
              if imag(y-n0)<detuningfactor
                     wopt(:,:,k)=w;
                      k=k+1;
               end
          end
       end
  end
end

% design reflectivity(rr) refining
s=size(wopt);
lambda=1300:1600;      %scanning range
j=1;
q=0;        %initial number of point, of which reflectivity<rr
for g=1:s(1,3)
  w(:,:)=wopt(:,:,g);
  d=w.*lambda0./4./n;          %film thickness, (quarter wavelength)
                                %(refinement factors)
  bc=bcfunction(n,d,lambda,nm);          %calculate [b;c], of which y=c/b
   roh=(n0-bc(2,1,:)./bc(1,1,:))./(n0+bc(2,1,:)./bc(1,1,:));
   for f=1:length(lambda);
       r(1,f)=roh(1,1,f);
   end
   reflectivity=r.*conj(r);
```

```
  m=0;          %number of point of which reflectivity<rr for a certain
                 %combination of [w]
  for k=1:length(reflectivity);
       if reflectivity(1,k)<rr;
            m=m+1;
       end
   end
  if m>30
    wopt1(j,:)=w(:,:);
    j=j+1       %as an indicator
  end
  if q<m
    q=m;
    wfin=w(:,:);
  end

end
wopt1=wopt1     % output wopt1
wfin=wfin       %output wfin
```

REFERENCES

[1] K.Kobayashi, and I.Mito, 'Single frequency and tunable laser diodes', J. Lightwave Technol., **6**, pp1623, 1988

[2] T.L.Koch, and U.Koren, 'Semiconductor lasers for coherent optical fiber communications', J. Lightwave Technol., **8**, pp274, 1990

[3] C.E.Wieman, and L.Hollberg, 'Using diode lasers for atomic physics', Rev. Sci. Instrum., **62**, pp1, 1991, and references therein

[4] R.W.Tkach and A.R.Chraplyvy, 'Regimes of feedback effect in 1.5µm distributed feedback lasers', J. Lightwave Technol., **LT-4**, pp1655, 1986

[5] H.S.Gingrich, D.R.Chumney, S.Z.Sun, S.D.Hersee, L.F.Lester, and S.R.J.Brueck, 'Broadly tunable external cavity laser diodes with staggered thickness multiple quantum wells', IEEE Photon. Technol. Lett., **9**, pp155, 1997

[6] X.Zhu, D.T.Cassidy, M.Hamp, D.Thompson, B.Robinson, Q.Zhao, and M.Davies, '1.4-µm InGaAsP-InP strained multiple-quantum-well laser for broad-wavelength tunability', IEEE Photon. Technol. Lett., **9**, pp1202, 1997

[7] L.Martinu, and D.Poitras, 'Plasma deposition of optical films and coatings: A review', J. Vac. Sci. Technol. A, **18**, pp2619, 2000, and references therein

[8] S.L.Chuang, *Physics of Optoelectronic Devices*, JOHN WILEY & SONS, 1995, Appendix K.3, p711

[9] B.R.Bennett, R.A.Soref, and J.A.D.Alamo, 'Carrier-induced change in refractive index of InP, GaAs, and InGaAsP', IEEE J. Quantum Electron., **26**, pp113, 1990

[10] D.Botteldooren, and R.Baets, 'Influence of band-gap shrinkage on the carrier-induced refractive index change in InGaAsP', Appl. Phys. Lett., **54**, pp1989, 1989

[11] M.A.Afromowitz, 'Refractive index of Ga_{1-x} Al_xAs', Solid State Commun., **15**, pp59, 1974

[12] P.Bhattacharya, ed., *Properties of III-V Quantum Wells and Superlattices*, INSPEC, 1996, p283-284

[13] H.Burkhard, 'Effective phase and group indices for $In_{1-x}Ga_xAs_yP_{1-y}$/InP waveguide structures', J. Appl. Phys, **55**, pp503, 1984

[14] J.Faist, F.K.Reinhart, D.Martin, and E.Tuncel, 'Orientation dependence of the phase modulation in a *p-n* junction GaAs/$Al_xGa_{1-x}As$ waveguide', Appl. Phys. Lett., **50**, pp68, 1987

[15] S.Adachi, 'Material parameters of $In_{1-x}Ga_xAs_yP_{1-y}$ and related binaries', J. Appl. Phys., **53**, pp8775, 1982

[16] M.Koshiba, *Optical Waveguide Analysis*, McGraw-Hill, Toronto, 1990

[17] H.Kogelnik, and V.Ramaswamy, 'Scaling rules for thin-film optical waveguides', Appl. Opt., **13**, pp1857, 1974

[18]L.M.Walpita, 'Solutions for planar optical waveguide equations by selecting zero elements in a characteristic matrix', J. Opt. Soc. Am. A, **2**, pp595, 1985

[19]G.Hocker, and W.Burns, 'Mode dipersion in diffused channel waveguides by the effective index method', Appl. Opt., **16**, pp113, 1977

[20]T.Mukai and Y.Yamamoto, 'Gain, frequency bandwidth, and saturation output power of AlGaAs DH laser amplifiers', IEEE J. Quantum Electron., **QE-17**, pp1028, 1981

[21]P.Zorabedian, 'Axial-mode instability in tunable external-cavity semiconductor lasers', IEEE J. Quantum Electron., **30**, pp1542, 1994

[22]T.Saitoh, T.Mukai, and O.Mikami, 'Theoretical analysis and fabrication of antireflection coatings on laser-diode facets', J. Lightwave Technol., **LT-3**, pp288, 1985

[23]B.Luo, L.Wu, J.Chen, and Y.Lu, 'Determination of wavelength dependence of the reflectivity at AR coated diode facets', IEEE Photon. Technol. Lett., **5**, pp1279, 1993

[24]W.Rideout, R.Holmstrom, J.LaCourse, E.Meland, and W.Powazinik, 'Ultra-low-reflectivity semiconductor optical amplifiers without antireflection coatings', Electron. Lett., **26**, pp36, 1990

[25]N.K.Dutta, A.B.Piccirilli, M.S.Lin, R.L.Brown, J.Wynn, D.Coblentz, Y.Twu, and U.K.Chakrabarti, 'Fabrication and performance characteristics of buried-facet optical amplifiers', J. Appl. Phys., **67**, pp3943, 1990

[26]P.E.Barnsley, J.J.Isaac, and D.J.Elton, 'Ultra-low reflectivity broadband 1.5 μm GaInAsP semiconductor optical amplifiers', Electron. Lett., **26**, pp825, 1990

[27]J.Buss, M.C.Farries, and D.J.Robbins, 'Reflectivity of coated and tilted semiconductor facets', IEEE J. Quantum Electron., **27**, pp1837, 1991

[28]A.Thelen, *Design of Optical Interference Coatings*, McGraw Hill, New York, 1989

[29]H.A.Macleod, *Thin-Film Optical Filters, 2nd*, Adam Hilger, Bristol, U.K., 1985

[30]E.Marclay, D.J.Webb, P.Buchmann, and P.Vettiger, 'Stepwise-graded-index multiplayer broadband low-reflectivity coating for AlGaAs/GaAs power lasers', Appl. Phys. Lett., **55**, pp942, 1989

[31]M.C.Farries, J.Buus, and M.Kearley, 'Design and fabrication of two layer antireflection coatings for semiconductor optical amplifiers', Electron. Lett., **26**, pp1626, 1990

[32]K.Shigihara, T.Aoyagi, S.Kakimoto, M.Aiga, M.Ostubo, and K.Ikeda, 'Antireflection coating for laser diodes', Electron. Lett., **31**, pp1574, 1995

[33]H.M.Liddell, *Computer-aided Techniques for the Design of Multilayer Filters*, Adam Hilger, Bristol, 1981

[34]J.T.Cox, 'Special type of double-layer antireflection coating for infrared optical materials with high refractive indices', J. Opt. Soc. Am., **51**, pp1406, 1961

[35] J.T.Cox, and G.Hass, *Antireflection Coatings for Optical and Infrared Optical Materials*, in *Physics of Thin Films*, G.Hass and R.E.Thun, ed., Academic, New York, 1964

[36] Such as, Software Spectra Inc., Portland, OR, 97229, www.sspectra.com

[37] J.L.Vossen, and W.Kern, ed., *Thin Film Processes II,* Academic Press Inc., 1993

[38] M.G.Boudreau, PhD thesis, McMaster University, 1997

[39] K.Wakita and S.Matsuo, 'Small surface damage facet coating on InGaAsP/InP laser by ECR plasma deposition', Jap. J. Appl. Phys., **23**, ppL556, 1984

[40] S.Dzioba and R.Rousina, 'Dielectric thin film deposition by electron cyclotron resonance plasma chemical vapor deposition for optoelectronics', J. Vac. Sci. Technol., B, **12**, pp433, 1994

[41] P.Longeway, *Semiconductors and Semimetals*, **21A**, Academic Press, New York, 1984, p179

[42] P.Mascher, M.G.Boudreau, S.G.Wallace, S.Murugkar, G.Balcaitis, Ch.Wettlaufer, and H.K.Haugen, 'Optical coatings for improved semiconductor diode laser performance', in: Light Emitting Devices for Optoelectronic Applications, ECS Proc. **98-2**, pp56, 1998

[43] H.R.Philipp, 'Optical properties of silicon nitride', J. Electrochem. Soc., **120**, pp295, 1973

[44] W.A.Pliskin, 'Refractive index dispersion of dielectric films used in the semiconductor industry', J. Electrochem. Soc., **134**, pp2819, 1987

[45] Paul Klocek ed., *Handbook of Infrared Optical Materials*, MARCEL DEKKER, 1991

[46] E.S.Bulat, G.Ditmer, C.Herrick, and S.Hankin, 'Characterization of biased electron cyclotron resonance deposited oxides', J. Vac. Sci. Technol., A, **10**, pp1402, 1992

[47] D.F.Edwards and E.Ochoa, 'Infrared refractive index of silicon', Appl. Opt., **19**, pp4130, 1980

[48] J.M.Essick, F.S.Pool, and Y.H.Shing, 'Deposition temperature dependence of the deep defect density for a-Si:H film grown by electron cyclotron resonance microwave plasma', J. Vac. Sci. Technol., A, **10**, pp521, 1992

[49] S.Callard, A.Gagnaire, and J.Joseph, 'Fabrication and characterization of graded refractive index silicon oxynitride thin films', J. Vac. Sci. Technol. A, **15**, pp2088, 1997

[50] A.E.T.Kuiper, S.W.Koo, F.H.P.M.Habraken, and Y.Tamminga, 'Deposition and composition of silicon oxynitride films', J. Vac. Sci. Technol. B, **1**, pp62, 1983

[51] D.E.Aspnes, J.B.Theeten, 'Dielectric function of Si-SiO_2 and Si-Si_3N_4 mixtures', J. Appl. Phys., **50**, pp4928, 1979

[52] P.G.Snyder, Y.M.Xiong, and J.A.Woollam, 'Graded refractive index silicon oxynitride thin film characterized by spectroscopic ellipsometry', J. Vac. Sci. Technol. A, **10**, pp1462, 1992

[53] V.N.Van, A.Brunet-Bruneau, S.Fisson, J.M.Frigerio, G.Vuye, Y.Wang, F.Abeles, J.Rivory, M.Berger, and P.Chaton, 'Determination of refractive-index profiles by a combination of visible and infrared ellipsometery measurements', Appl. Opt., **35**, pp5540, 1996

[54] P.V.Bulkin, P.L.Swart, and B.M.Lacquet, 'Properties and applications of electron cyclotron plasma deposited SiO_xN_y films with graded refractive index profiles', Journal of Non-Crystalline Solids, **187**, pp484, 1995

[55] H.G.Tompkins, R.B.Gregory, P.W.Deal, and S.M.Smith, 'Analysis of silicon oxynitrides with spectroscopic ellipsometry and Auger spectroscopy, compared to analyses by Rutherford backscattering spectrometry and Fourier transform infrared spectroscopy', J. Vac. Sci. Technol. A, **17**, pp391, 1999

[56] H.G.Tompkins, *A User's Guide to Ellipsometry*, Academic Press Inc., 1993

[57] F.L.Pedrotti, and L.S.Pedrotti, *Introduction to Optics*, *2nd* , Prentice Hall, New Jersey, 1993, a.Chapter 20; b.Chapter 17; c.Chapter 22

[58] Operation manual for Rotating Compensator Fourier Ellipsometer, *Model i1000, Rudolph Research Systems*

[59] R.Wyatt, and W.R.Devlin, '10kHz linewidth 1.5 μm InGaAsP external cavity laser with 55 nm tuning range', Electron. Lett., **19**, pp110, 1983

[60] I.P.Kaminow, G.Eisenstein, and L.W.Stulz, 'Measurement of the modal reflectivity of an antireflection coating on a superluminescent diode', IEEE J. Quantum Electron., **QE-19**, pp493, 1983

[61] D.T.Cassidy, 'Technique for measurement of the gain spectra of semiconductor diode lasers', J. Appl. Phys., **56**, pp3096, 1984

[62] B.W.Hakki and T.L.Paoli, 'Gain spectra in GaAs double-heterostructure injection lasers', J. Appl. Phys., **46**, pp1299, 1975

[63] S.A.Merritt, D.S.Fox, I.F.Wu, and M.Dagenais, 'Measurement of the facet modal reflectivity spectrum in high quality semiconductor traveling wave amplifiers', J. Lightwave Technol., **13**, pp430, 1995

[64] L.A.Lam Sin Cho, P.M.Smowton, and B.Thomas, 'Spectral gain measurements for semiconductor laser diodes', IEE Proceedings, Pt.J, **137**, pp64, 1990

[65] K.Petermann, 'External optical feedback phenomena in semiconductor lasers', IEEE Journal of Selected Topics in Quantum Electronics, **1**, pp480, 1995

[66] D.Lenstra, B.H.Verbeek, and A.J.D.Boef, 'Coherence collapse in single-mode semiconductor lasers due to optical feedback', IEEE J. Quantum Electron., **QE-21**, pp674, 1985

[67] A.H.Nguyen, PhD thesis, McMaster University, 1999

[68] L.J.Bonnell, and D.T.Cassidy, 'Alignment tolerances of short-external-cavity InGaAsP diode lasers for use as tunable single-mode sources', Appl. Opt., **28**, pp4622, 1989

[69] C.Voumard, R.Salathe, and H.Weber, 'Resonance amplifier model describing diode lasers coupled to short external resonators', Appl. Phys., **12**, pp369, 1977

[70] C.H.Henry, and R.F.Kazarinov, 'Stabilization of single frequency operation of coupled-cavity lasers', IEEE J. Quantum Electron., **QE-20**, pp733, 1984

[71] X.Zhu, PhD thesis, McMaster University, 1996, Chapter 2

[72] such as, Grating Solver, Allen, TX, 75013, www.gsolver.com

[73] G.W.Stroke, *Diffraction Gratings*, in *Encyclopedia of Physics*, **29**, S.Flugge, ed., Springer-Verlag, Berlin, 1967, pp433-609

[74] P.Zorabedian, *Tunable External-Cavity Semiconductor Lasers*, in *Tunable Lasers Handbook*, F.J.Duarte, ed., Academic Press, 1995

[75] E.G.Loewen, M.Neviere, and D.Maystre, 'Grating efficiency theory as it applies to blazed and holographic gratings', Appl. Opt., **16**, pp2711, 1977

[76] B.Tromborg, H.Olesen, X.Pan, and S.Saito, 'Transmission line description of optical feedback and injection locking for Fabry-Perot and DFB lasers', IEEE J. Quantum Electron., **QE-23**, pp1875, 1987

[77] Y.Li, and J.Katz, 'Nonparaxial analysis of the far-field radiation patterns of double-heterostructure lasers', Appl. Opt., **35**, pp1442, 1996

[78] G.P.Agrawal, 'Longitudinal-mode stabilization in semiconductor lasers with wavelength selective feedback', J. Appl. Phys., **59**, pp3958, 1986

[79] A.Olsson, and C.L.Tang, 'Coherent optical interference effects in external-cavity semiconductor lasers', IEEE J. Quantum Electron., **QE-17**, pp1320, 1981

[80] C.Yan, X.Wang, and J.G.McInerney, 'Multistability in grating-tuned external-cavity semiconductor lasers', IEEE J. Quantum Electron., **32**, pp813, 1996

[81] Such as, Sacher Lasertechnik, Germany, www.sacher-laser.com

[82] C.F.Lin, Y.S.Su, and B.R.Wu, 'External-cavity semiconductor laser tunable from 1.3 to 1.54 μm for optical communication', IEEE Photon. Technol. Lett., **14**, pp3, 2002

[83] D.Mehuys, M.Mittelstein, A.Yariv, R.Sarfaty, and J.E.Ungar, 'Optimized Fabry-Perot (AlGa)As quantum-well lasers tunable over 105 nm', Electron. Lett., **25**, pp143, 1989

[84] J.E.Fouquet, D.M.Braun, and G.R.Trott, 'Wavelength-dependent optimum output coupling enhances performance of external-cavity-tuned semiconductor laser at 1.5μm', IEEE J. Quantum Electron., **32**, pp1777, 1996

[85] Y.S.Shin, T.H.Yoon, J.R.Park, and C.H.Nam, 'Simple methods for measuring the linewidth enhancement factor in external cavity laser diodes', Opt. Commun., **173**, pp303, 2000